Biophysical Journal, Volume *111*

Supplemental Information

Identification of Bifurcations from Observations of Noisy Biological Oscillators

Joshua D. Salvi, Dáibhid Ó Maoiléidigh, and A.J. Hudspeth

SUPPORTING MATERIAL

Identification of bifurcations from observations of noisy biological oscillators

Joshua D. Salvi, Dáibhid Ó Maoiléidigh, and A. J. Hudspeth*

Howard Hughes Medical Institute and Laboratory of Sensory Neuroscience
The Rockefeller University
1230 York Avenue, New York, NY, 10065, USA

*Correspondence: hudspaj@rockefeller.edu

Table of Contents

List of Figures

Preface

This document is a self-contained guide to the methods presented in the accompanying paper. We hope that this Supporting Material will benefit those who may wish to employ similar methodology for identification and location of bifurcations in noisy systems. The Supporting Material is organized as follows:

- **Section A: The Mechanical-Load Clamp.** We describe the theoretical foundation and implementation of a feedback-based clamp system to control the mechanical loads delivered to individual biological oscillators.
- **Section B: The Hair Bundle's State Diagram.** Having verified the mechanical-load clamp, we used this system to systematically deliver loads to individual hair bundles. This allowed us to generate a state diagram, a two-dimensional map of bundle behavior as a function of these loads.
- **Section C: Analytical Metrics.** We describe here the tools and metrics used to identify the types and locations of bifurcations near which a dynamical system might operate.
- **Section D: Noisy Simulations of Bifurcation Normal Forms.** The behavior of a system operating near a bifurcation can be reduced to a simple mathematical representation: a normal form. Here we describe each of the normal forms used in this study and provide details on how stochastic simulations were performed.
- **Section E: Noisy Simulations of a Model of Hair-Bundle Mechanics.** We describe here a qualitative model of hair-bundle mechanics that captures the dynamics of bundles across organs and species. We include details on how the simulations were performed and provide examples of the model's output.
- **Section F: Analysis of Hair Bundles in the Presence of Noise.** We provide additional details on the two classes of hair-bundle behavior and the bifurcations that correspond to these classes.
- **Section G: Noise-Induced Spiking in a Model of Hair Bundle Mechanics.** We show that a model hair bundle crossing a subcritical Hopf bifurcation displays spiking behavior resembling that of a system operating near a SNIC bifurcation.

SECTION A

The Mechanical-Load Clamp

To control the mechanical loads applied to individual hair bundles, we designed and implemented a mechanical-load clamp [1, 2]. The load clamp permits robust control of the constant force, stiffness, drag coefficient, and mass of a mechanical load. Rather than physically exchanging mechanical objects coupled to individual bundles, the bundle's load can be adjusted using only a feedback-based circuit. Here we describe both the mathematical foundation and the experimental verification of a mechanical-load clamp.

A.1 Mathematical Description

A hair bundle's mechanical load controls its function [2, 3]. This load may include a constant force, a stiffness, a drag, and a mass. The behavior of a hair bundle under different combinations of these loads can be captured by a map: a state diagram. One may thus envision an experimental system that—analogously to accessory structures *in vivo*—imposes mechanical loads to adjust the behavior of an active hair bundle. Such a system would allow characterization of a bundle's behavior throughout its state diagram. We earlier developed a feedback-based mechanical-load clamp; here we describe an extension to the system to encompass not only an external force and virtual stiffness but also a virtual drag and virtual mass.

The equation of motion for a hair bundle coupled to a flexible stimulus fiber is

$$m_B\ddot{X} + \xi_B\dot{X} + K_BX - F_A = -\xi_{XX}\dot{X} - \xi_{\Delta X}\dot{\Delta} + K_F(\Delta - X), \tag{S1}$$

in which X is the position of the hair bundle and m_B, ξ_B, and K_B are respectively its mass, drag coefficient, and stiffness. $\dot{X}$ and $\ddot{X}$ correspond to respectively the bundle's velocity and acceleration. The term F_A represents the bundle's active force. Δ and $\dot{\Delta}$ are the position and velocity of the stimulus fiber's base, K_F is the fiber's stiffness, ξ_{XX} is the drag coefficient owing to motion at the fiber's tip, and $\xi_{\Delta X}$ is that owing to motion of the fiber's base.

We measured the bundle's position by tracking the shadow of the fiber's tip, magnified and projected onto a dual-photodiode system, which generated a voltage $V_D = \alpha X$. To calculate the coefficient α, we displaced the shadow of the fiber's tip with a piezoelectric actuator in 20 µm steps. In a feedback-based position clamp, an error signal was generated in proportion to the difference between the bundle's actual position X and a commanded position X_C: $V_E = V_C - V_D = \alpha(X_C - X)$. This error signal was relayed through a differential amplifier and multiplied by a proportional gain G to generate an output voltage $V_O = GV_E$. This output signal was then directed to another piezoelectric actuator that controlled the motion of the stimulus fiber's base. The relationship between the error signal and the motion of the base of the stimulus fiber is

$$\Delta = \beta V_O = \beta G V_E = \beta G(V_C - V_D) = \alpha\beta G(X_C - X). \tag{S2}$$

The calibration term β describes the relationship between the input voltage to the piezoelectric actuator that controls the fiber's base and its resulting motion.

We can next suppose the bundle is loaded with a virtual mass m_V, a virtual drag ξ_V, stiffness K_L, and external force F_E. The external force can be considered a sum of a constant force F_C and a stimulus force F_S, $F_E = F_C + F_S$. The bundle's equation of motion then becomes

$$m_B\ddot{X} + \xi_B\dot{X} + K_B X - F_A = -m_V\ddot{X} - \xi_V\dot{X} - K_L X + F_C + F_S. \tag{S3}$$

By combining Equations S1 and S3, we obtain a relation describing the capacity of the mechanical-load clamp to deliver loads to individual hair bundles:

$$-\xi_{XX}\dot{X} - \xi_{\Delta X}\dot{\Delta} + K_F(\Delta - X) = -m_V\ddot{X} - \xi_V\dot{X} - K_L X + F_C + F_S. \tag{S4}$$

We must now calculate the value of the commanded position X_C required to deliver these virtual mechanical loads. This is achieved by combining Equations S2 and S4, yielding

$$\alpha\beta G\left(\xi_{\Delta X}\dot{X}_C - K_F X_C\right) = m_V\ddot{X} + (\xi_V - \xi_{XX} + \alpha\beta G\xi_{\Delta X})\dot{X} + \left[K_L - (1+\alpha\beta G)K_F\right]X - F_C - F_S. \tag{S5}$$

A real-time processor discretizes equation S5 with time intervals δt of equal duration. Estimates of the bundle's instantaneous velocity and acceleration at index j therefore become

$$\dot{X}_j = \frac{X_j - X_{j-1}}{\delta t}, \tag{S6}$$

$$\ddot{X}_j = \frac{X_j - 2X_{j-1} + X_{j-2}}{\delta t}. \tag{S7}$$

Combining Equations S5-S7 yields the command signal $V_{C,j}$ at the j^{th} time interval:

$$\begin{aligned} V_{C,j} = {} & \frac{\xi_{\Delta X} V_{C,j-1}}{\xi_{\Delta X} - K_F\delta t} \\ & + \left(\frac{m_V\ddot{X}_j + (\xi_V - \xi_{XX} + \alpha\beta G\xi_{\Delta X})\dot{X}_j + \left[K_L - (1+\alpha\beta G)K_F\right]X_j - F_{C,j} - F_{S,j}}{\beta G(\xi_{\Delta X} - K_F\delta t)}\right)\delta t. \end{aligned} \tag{S8}$$

Given a set of inputs G, m_V, ξ_V, K_L, F_C, and F_S, the mechanical-load clamp calculated for each time interval an appropriate command voltage according to Equation S8. For experiments in this study, we controlled only the load stiffness and constant force applied to an individual hair bundle, setting m_V, ξ_V, and sometimes F_S equal to zero.

Our experiments employed fibers with typical stiffnesses of $K_F = 100 - 300\ \mu\mathrm{N} \cdot \mathrm{m}^{-1}$ and drag coefficients of $\xi_{XX} = 130 - 250\ \mathrm{nN} \cdot \mathrm{s} \cdot \mathrm{m}^{-1}$ and $\xi_{\Delta X} = 80 - 150\,\mathrm{nN} \cdot \mathrm{s} \cdot \mathrm{m}^{-1}$ [4]. The gain G was typically 0.01-0.1.

For our experiments we computed the complete Equation S8 at each index j. This allowed us to avoid the need for assumptions regarding the bundle's drag coefficients that were required in our previous study [2]. Moreover, we previously adjusted the command voltage V_C and gain G to change the mechanical load. Here we varied only the command voltage V_C to control the load, resulting in an increase in the load clamp's stability.

A.2 Verification of the Mechanical-Load Clamp

We verified that the mechanical-load clamp successfully imposes a load stiffness and constant force on a hair bundle. To do so, we coupled the tip of a flexible glass stimulus fiber to the tip of a vertically mounted glass fiber that served as a model hair bundle. We then delivered force pulses of different amplitudes in the presence of a range of virtual load stiffnesses. This yielded a relationship that accorded with the behavior of a Hookean material (Fig. S1).

To assess the clamp's effect on spontaneously active hair bundles, we coupled the tip of a stimulus fiber to the kinociliary bulb of an active bundle from the bullfrog's sacculus. In keeping with our theoretical predictions and prior work [2, 3], a hair bundle's spontaneous oscillations decreased in amplitude and increased in frequency as the load stiffness rose (Fig. S2A). Another bundle initially exhibited multimodal oscillations for small values of load stiffness. Upon an increase in the stiffness, both the fast and slow modes of oscillation increased in frequency and decreased in amplitude until oscillations ceased altogether at a load stiffness of $500\ \mu\mathrm{N} \cdot \mathrm{m}^{-1}$ (Fig. S2B).

Finally, we assessed a simulated load clamp's effect on a model hair bundle. To do so, we performed simulations of a model of hair-bundle dynamics when coupled to a mechanical-load clamp:

$$\dot{X} = -K_B X + a(X - f) - (x - f)^3 + F_O + F_F, \tag{S9}$$

$$\tau_f \dot{f} = bx - f, \tag{S10}$$

$$F_F = K_F \left[\alpha\beta G(X_C - X) - X\right], \tag{S11}$$

in which $X_C = V_C/\alpha$ and V_C is described by Equation S8. Here a is a stiffness, F_O is the bundle's intrinsic offset force, F_F is a force exerted by the stimulus fiber onto the bundle, f is the bundle's force of adaptation, τ_f is the time constant of adaptation, and b is a stiffness. Because the model of hair-bundle dynamics has been rescaled, we additionally rescaled the load clamp's unitless parameters to exert forces of an appropriate order of magnitude. For these simulations, $a = 3.5$, $K_B = F_O = 0$, $\tau_f = 10$, $b = 0.5$, $\alpha = 10$, $\beta = 0.1$, $G = 1$, $K_F = 1$, and drag owing to the fiber has been neglected. We integrated Equations S9-S11 numerically in MATLAB (R2014a) with the Euler-Murayama method using a time step of 10^{-2} for combinations of 41 values each of constant force and load stiffness.

We calculated the amplitude and frequency of the model hair bundle's spontaneous oscillations from the largest peak in each power spectrum. Operating points for which the bundle's oscillations fell below an amplitude of 10^{-2} and displayed only single peaks in their position histograms were classified as non-oscillatory. This approach produced an artificial state diagram that agreed with theoretical predictions (Fig. S3). As the load stiffness increased, the bundle's oscillation amplitude fell and its frequency of spontaneous oscillation rose. The oscillatory region followed closely the lines of supercritical and subcritical Hopf bifurcations for this set of parameters [3]. Both in experiments and in simulations, the mechanical-load clamp therefore controlled the constant force and load stiffness applied to a hair bundle.

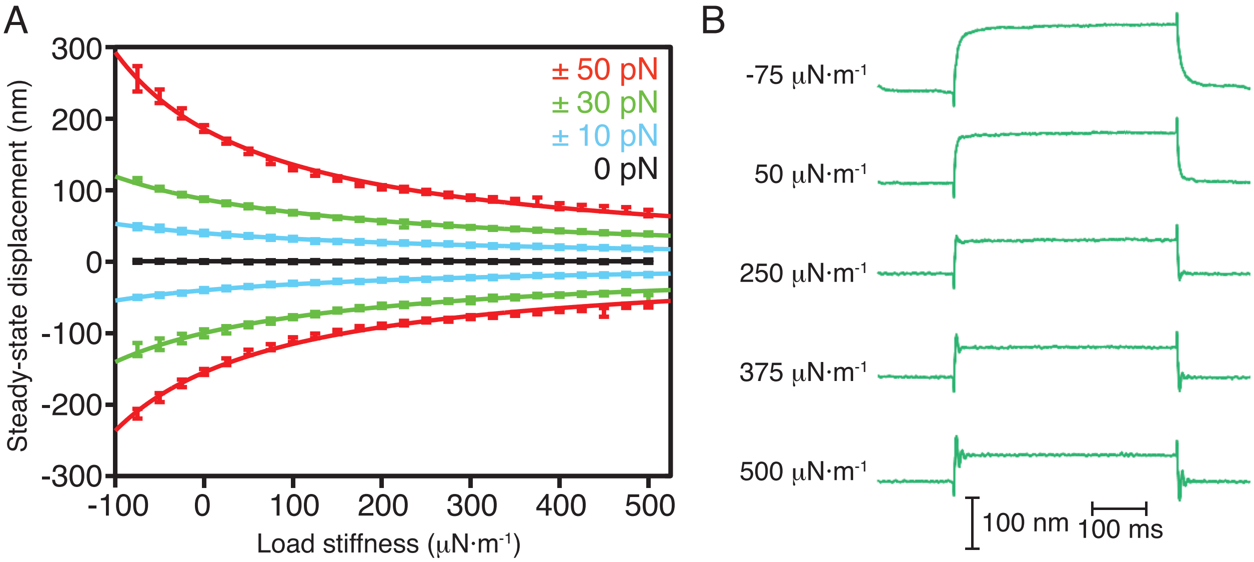

Figure S1: **Control of constant force and load stiffness with a mechanical-load clamp**. (A) To verify that a load clamp can adjust a bundle's virtual stiffness and constant force, we coupled the tip of a glass stimulus fiber to a vertically mounted fiber and delivered a series of constant forces ($F_C = 0, \pm 10, \pm 30, \pm 50$ pN) at different values of load stiffness ($-100\ \mu\mathrm{N}\cdot\mathrm{m}^{-1} \leq K_L \leq 500\ \mu\mathrm{N}\cdot\mathrm{m}^{-1}$). Fits to the expression $X = F_C/\left(K_L + K_B\right)$ yielded $R^2 > 0.99$ in all cases. (B) Example traces for the experiment in (A) at $F_C = 30$ pN revealed a change in the rise time of the fiber's step response: as the load stiffness increased, the rise time declined. For load stiffnesses exceeding 250 $\mu\mathrm{N}\cdot\mathrm{m}^{-1}$, the response rang with a decay time that grew with the stiffness owing to the mass of the vertically mounted fiber. These phenomena accord with the prediction that the fiber's virtual stiffness increased. In all panels, $m_V = \xi_V = F_C = 0$ and $G = 0.01$.

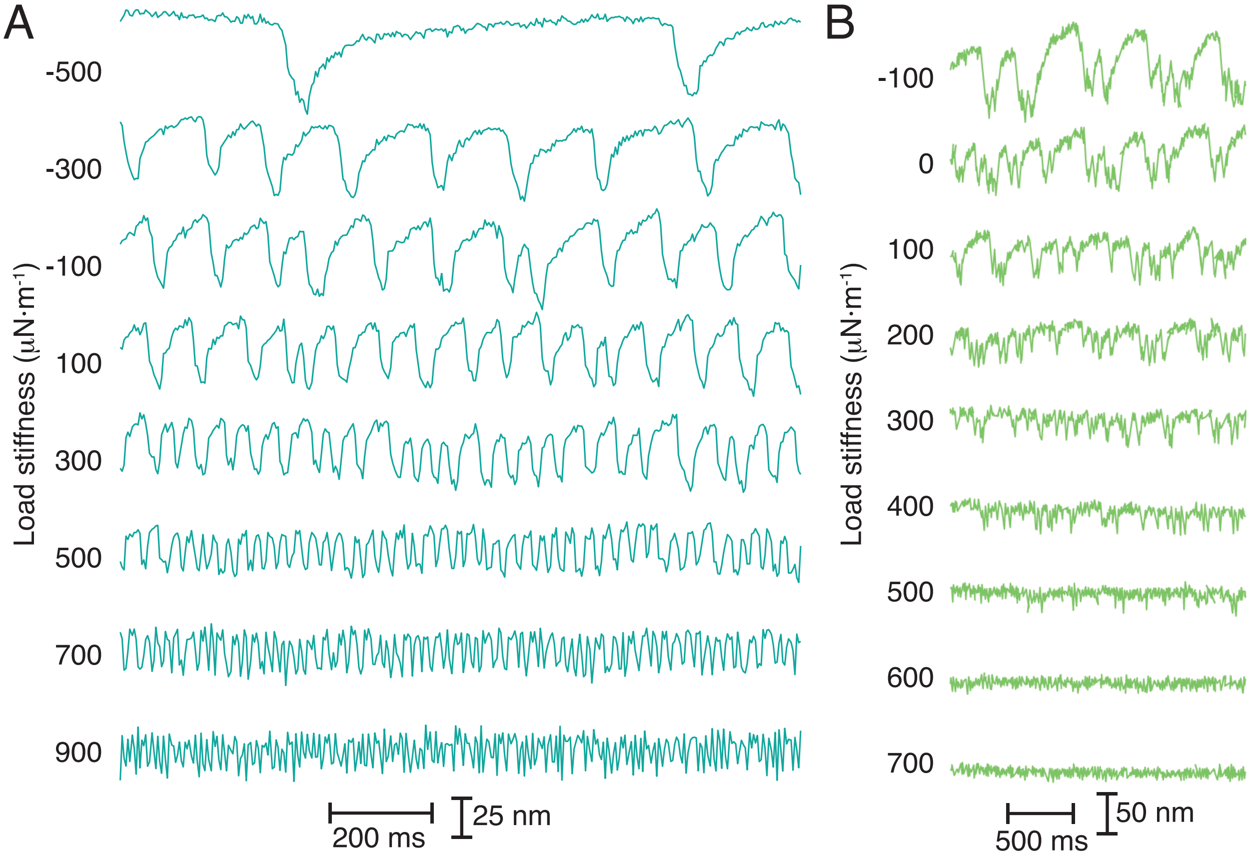

Figure S2: **Hair-bundle motion as a function of changes in load stiffness**. (A) We subjected a spontaneously oscillating hair bundle to load stiffnesses of -500 $\mu\mathrm{N}\cdot\mathrm{m}^{-1}$ through 900 $\mu\mathrm{N}\cdot\mathrm{m}^{-1}$. As the stiffness increased, the bundle's oscillations rose in frequency and declined in amplitude. At a load stiffness of -500 $\mu\mathrm{N}\cdot\mathrm{m}^{-1}$, the bundle resided mostly at a positive position with a downward excursion occurring approximately every 700 ms. (B) Imposing on another hair bundle load stiffnesses ranging from -100 $\mu\mathrm{N}\cdot\mathrm{m}^{-1}$ through 700 $\mu\mathrm{N}\cdot\mathrm{m}^{-1}$ disclosed a similar pattern in amplitude and frequency. Load stiffnesses exceeding 500 $\mu\mathrm{N}\cdot\mathrm{m}^{-1}$ suppressed the hair bundle's oscillations. The total acquisition time under each condition was 30 s at a sampling interval of 200 μs. The stimulus fiber possessed a stiffness of 150 $\mu\mathrm{N}\cdot\mathrm{m}^{-1}$ and a drag coefficient of 100 $\mathrm{nN}\cdot\mathrm{s}\cdot\mathrm{m}^{-1}$. In all panels, $m_V = \xi_V = F_C = 0$ and $G = 0.01$.

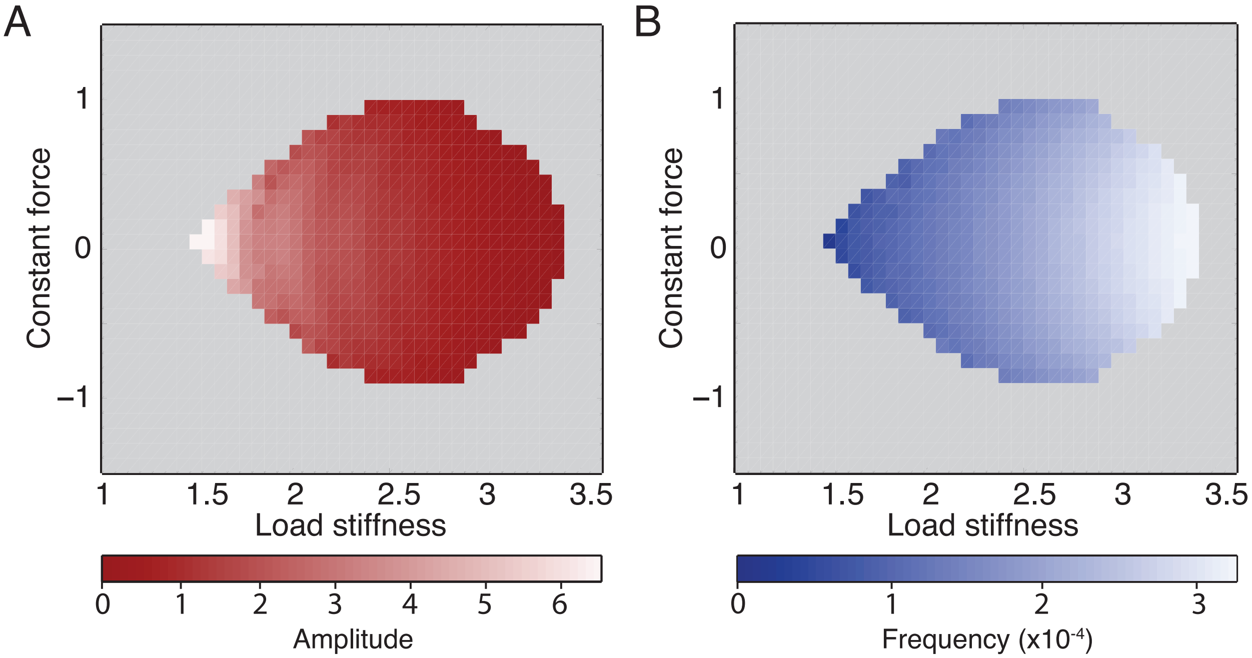

Figure S3: **Exploration of a model bundle's state diagram with a simulated load clamp**. (A) We set both the intrinsic offset force and the stiffness of a hair bundle to zero and adjusted the constant force and load stiffness applied with a virtual mechanical-load clamp. The resultant oscillatory region (red) bounded by a domain of quiescence (gray) resembled that of a bundle's theoretical state diagram (Fig. 1A). An increase in load stiffness caused a decrease in the amplitude of spontaneous oscillation. (B) The frequency of oscillation rose with an increase in load stiffness (blue).

SECTION B

The Hair Bundle's State Diagram

We used the mechanical-load clamp from Section A to control the loads applied to hair bundles of the bullfrog's sacculus. By changing the constant force and load stiffness applied to a bundle, we generated a map of the bundle's behavior—a state diagram—as a function of these two control parameters. Here we describe the statistical methods by which we classified a hair bundle's behavior as either spontaneously oscillatory or quiescent and calculated an oscillating bundle's amplitude and frequency of motion. We include the results of these measures for an individual hair bundle.

B.1 Preparation of an Experimental State Diagram

A state diagram captures the behavior of a hair bundle when coupled to different mechanical loads. We employed a mechanical-load clamp to apply loads to an individual hair bundle and recorded the bundle's position for 12 s at each operating point. From the results we could map the bundle's experimental state diagram.

For a given combination of constant force and load stiffness, a hair bundle could either oscillate spontaneously or remain quiescent. To classify a bundle's behavior, we assessed its position histogram at each operating point. If the bundle oscillated with an amplitude that exceeded the level of noise, its distribution of positions displayed at least two peaks. If the bundle instead remained quiescent or possessed oscillations indistinguishable from noise, its position distribution displayed only one. We therefore quantified the modality of the bundle's position histogram at each operating point, in which unimodal and multimodal distributions corresponded respectively to quiescent and oscillatory behavior.

Hartigans' dip statistic evaluates the modality of a distribution, with a low value reflecting a unimodal distribution [5]. To calculate the dip statistic for each combination of constant force and load stiffness, we first removed the slow drift in a time series by subtracting from it the data smoothed with a moving average with a window 1 s in width. We then eliminated high-frequency noise by applying another moving average with a window of 0.02 s in width. These procedures represented the equivalent of band-pass filtering with cutoff frequencies of 1 Hz and 50 Hz. The dip statistic was subsequently calculated from the bundle's position histogram binned according to the Freedman-Diaconis rule [6]. We tested the distribution against a null uniform distribution possessing the same mean, variance, and length as that of the experimental record. We then classified as oscillatory all operating points possessing a dip statistic of at least 0.01 and a p-value below 10^{-3}.

We employed two methods to estimate the amplitude and frequency of the bundle's spontaneous oscillations. First, we measured these values from the peak of the time series' Fourier transform. The unfiltered trace of bundle motion was multiplied by a Hamming window, mean-subtracted, and zero-padded to reduce spectral leakage and improve precision in determining the peak. Because the time series was filtered for calculation of the dip statistic, we searched for peaks across a range of 1-50 Hz. The peak's value was then rescaled by a factor calculated by applying the same procedure to a sinusoidal waveform of the same length as the original time series.

Because the Fourier transform of noisy hair-bundle motion sometimes possessed many peaks due to phase slips, changes in oscillatory frequency, and other factors, we additionally employed a peak-detection algorithm to calculate the bundle's amplitude and frequency of oscillation [7]. By finding the locations of all peaks and troughs in the time series of bundle motion, we calculated the frequency as the inverse of the mean inter-peak interval and the amplitude as half of the mean difference between each peak and trough. We tested the algorithm over a range of thresholds between the maximum noise floor and the maximum amplitude of spontaneous oscillation. Here we selected a threshold of 25 nm, which rested in the middle of this range and yielded values consistent with observations of the bundle's time-series data. Together, these methods provided two experimental state diagrams for an individual hair bundle.

B.2 Results

We subjected a hair bundle with a diameter of 4 µm from the bullfrog's sacculus to 81 combinations of constant force ranging from -80 pN to +80 pN and load stiffness from $200\,\mu\mathrm{N}\cdot\mathrm{m}^{-1}$ to $1000\,\mu\mathrm{N}\cdot\mathrm{m}^{-1}$. The hair bundle oscillated spontaneously at 60 of these operating points, resulting in an experimental state diagram with an ovoid oscillatory regime surrounded by a domain of quiescence (Fig. S4). For state diagrams calculated from a peak-detection algorithm and the Fourier transform of the time series, the bundle's amplitude fell and its frequency of oscillation rose with an increase in load stiffness. We found that the bundle's frequency of motion calculated from the Fourier transform varied over the same range of values as the frequency calculated from the peak-detection algorithm. However, due to the presence of multiple peaks in the bundle's amplitude spectrum, the amplitudes of oscillation calculated from the Fourier transform were about one-quarter of those calculated by peak detection and the frequencies of oscillation were much more variable as the control parameter was changed than those found using the peak-detection algorithm. Owing to the variability in the frequency of oscillation calculated using the Fourier transform, the correlation between the frequency of oscillation and load stiffness was statistically significant for only the peak-detection algorithm (Table S1).

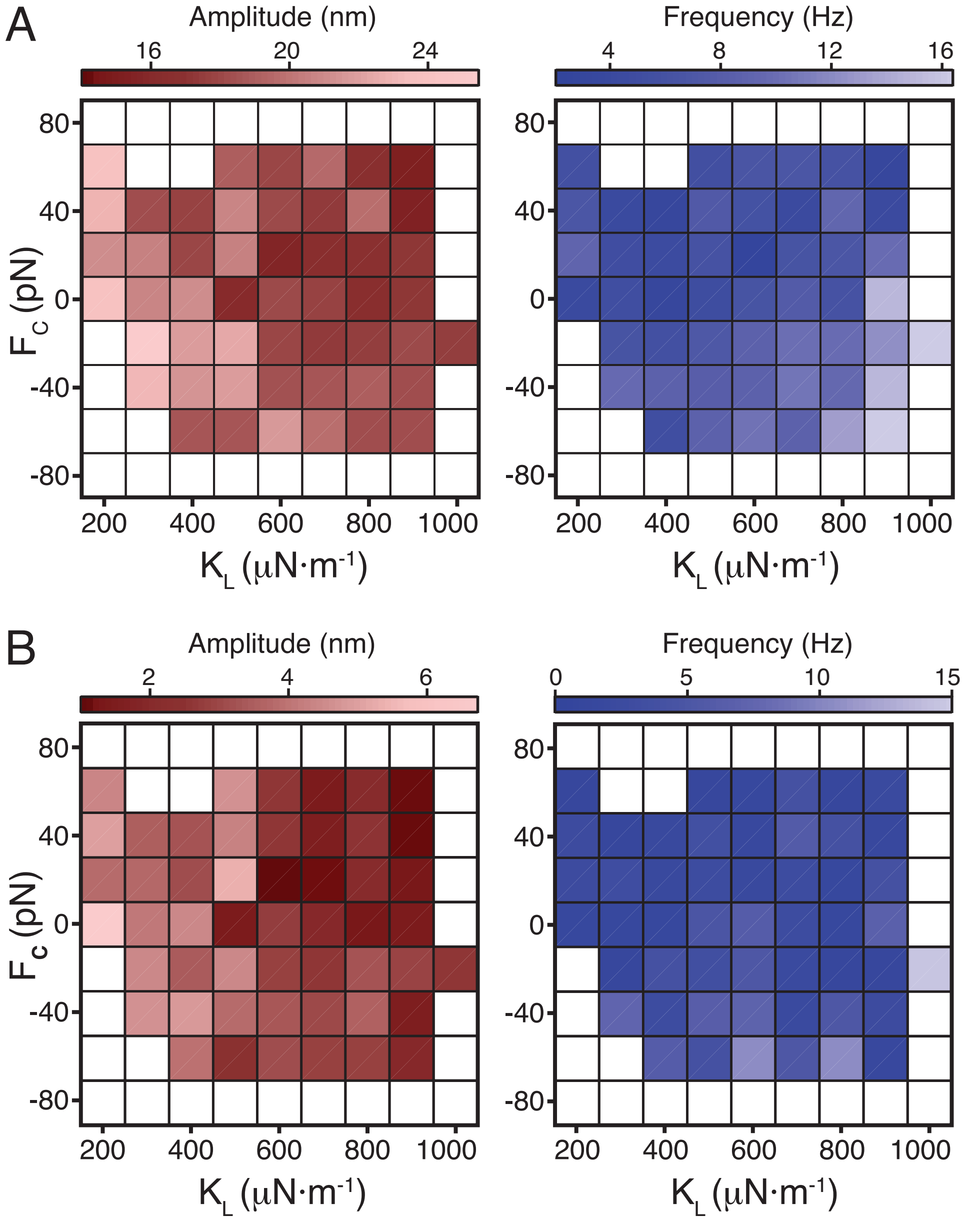

Figure S4: **A hair bundle's experimental state diagram.** (A) A hair bundle oscillated spontaneously for combinations of constant force (F_C) and load stiffness (K_L) within an oscillatory regime (colored) bounded by a region of quiescence (white). The amplitude and frequency of oscillation calculated with a peak-detection algorithm are displayed respectively in shades of red and blue. (B) The same bundle's experimental state diagram displayed similar patterns in amplitude and frequency when they were calculated from the Fourier transform of the time series of bundle motion.

PEAK DETECTION

	Ampl. *vs* $\mathbf{K_L}$	**Freq. *vs* $\mathbf{K_L}$**	Ampl. *vs* $\mathrm{F_C}$	**Freq. *vs* $\mathbf{F_C}$**	Ampl. *vs* Freq.
Spearman's ρ	**-0.67**	**0.48**	-0.24	**-0.56**	0.07
p-value	**7.4 x 10^{-8}**	**4.1 x 10^{-4}**	8.4 x 10^{-2}	**1.7 x 10^{-5}**	6.3 x 10^{-1}

FOURIER TRANSFORM

	Ampl. *vs* $\mathbf{K_L}$	Freq. *vs* $\mathrm{K_L}$	Ampl. *vs* $\mathrm{F_C}$	**Freq. *vs* $\mathbf{F_C}$**	Ampl. *vs* Freq.
Spearman's ρ	**-0.74**	0.13	-0.15	**-0.45**	-0.08
p-value	**3.9 x 10^{-10}**	3.5 x 10^{-1}	2.9 x 10^{-1}	**8.8 x 10^{-4}**	5.6 x 10^{-1}

Table S1: **Correlations within the bundle's experimental state diagram.** Spearman's ρ quantifies the correlations between the amplitude or frequency of oscillation and the constant force (F_C) or load stiffness (K_L). The values of Spearman's ρ and its associated p-value are shown for results from the peak-detection algorithm and from the Fourier transform of the time series. Columns in bold represent cases for which $p < 10^{-3}$.

Section C

Analytical Metrics

We employed several metrics to characterize the behavior of a noisy dynamical system operating near one or more bifurcations. Using these metrics, we hoped to classify the system according to the type of bifurcation near which it operates and to estimate the value of the control parameter at which the bifurcation resides. We estimated the location of a bifurcation from Hartigans' dip statistic for the distribution of positions in the time series, from the coefficient of variation for the distribution of times between successive peaks or troughs, and from the mutual information between the real and imaginary components of the analytic signal of a time series. In addition to the above metrics, we classified the type of bifurcation from the joint probability distribution of the real-valued positions of the system and its Hilbert transform and from the amplitude and frequency of the system's spontaneous motion.

We include here a set of tools that requires few manual choices by an experimenter. An experimenter should also be able to employ these metrics with ease, encountering little difficulty in either interpretation or implementation. Finally, we sought methods that can be applied to a system—such as a hair bundle—operating in an environment with substantial noise and whose time series may be of limited length.

C.1 Hartigans' Dip Statistic

A system that exhibits limit-cycle oscillations that can be distinguished from noise possesses a distribution of time-series values with more than one peak. As a measure of the onset of spontaneous oscillations, we therefore employed Hartigan's dip statistic, whose high and low values correspond respectively to multimodal and unimodal distributions. For an empirical probability density function $f(x)$ and its cumulative distribution function $F(x)$, the dip statistic is

$$D(F) = \inf_{H \in \mathcal{U}} \left[\sup_{x} |F(x) - H(x)| \right], \tag{S12}$$

in which H is a member of a family of cumulative distribution functions $\mathcal{U}$ arising from unimodal probability density functions, $\inf\limits_{H \in \mathcal{U}}$ is the infinum for all distributions H that are members of $\mathcal{U}$, and $\sup\limits_{x}$ corresponds to the supremum across all values of x. The maximum value of $D(F)$ is 0.25, corresponding to a maximally bimodal probability density function [5].

For stochastic simulations it was not necessary to detrend or filter the data prior to calculation of the dip statistic. For experimental time series of bundle motion, we detrended the data by subtracting the smoothened time series calculated from a moving average with a window of a length equal to half that of the time series (typically 8-30 s). Error bars from stochastic simulations represent the standard errors of the means from five time series, and those from experimental data represent standard errors calculated from 10^4 bootstrap samples. We calculated the dip statistic's p-value by comparing the dip statistic from the empirical distribution to a distribution of dip statistics drawn from $5 \cdot 10^3$ uniformly-distributed arrays, each of the same length as the original signal. Time-series data yielding $p < 10^{-3}$ were classified as oscillatory and all others as non-oscillatory.

C.2 The Analytic Distribution

The phase portrait of a dynamical system reveals fixed points and limit cycles that may be either stable or unstable. Under experimental conditions one may reconstruct an n-dimensional phase space by embedding the system's trajectory in these dimensions [8, 9]. Although this approach works in principle, phase-space embedding requires the specification of several parameters, such as the number of dimensions and a time delay [10, 11, 12]. Because these methods depend upon a number of decisions made by an experimenter and are at times difficult to employ and interpret, we instead used the Hilbert transform to reconstruct a map similar to a phase space. A real-valued signal and its Hilbert transform permit embedding of data into a two-dimensional phase space [13, 14, 15]. The analytic distribution is the joint probability distribution between the real and imaginary parts of the analytic signal. This method does not require the selection of any parameter values and can reveal both limit cycles and fixed points.

We define the Hilbert transform of a real-valued signal $X(t)$ as

$$X_H(t) = \mathcal{F}^{-1}\left[-i \cdot \operatorname{sgn}(\omega) \cdot \tilde{X}(\omega)\right], \tag{S13}$$

in which $\mathcal{F}^{-1}\left[f(x)\right]$ is the inverse Fourier transform of the function $f(x)$, $i = \sqrt{-1}$, $\operatorname{sgn}(\omega)$ is the sign function of the frequency ω, and $\tilde{X}(\omega)$ is the Fourier transform of $X(t)$. We can then generate the analytic distribution as the joint probability distribution of $X(t)$ and $X_H(t)$. For this paper, we calculated this distribution with a total of 2^8-2^{11} equal-width bins. In the presence of limit-cycle oscillations, the distribution yielded a circle or oval. The absence of limit-cycle oscillations instead revealed a unimodal density. Finally, fixed points within, on, or near a limit cycle appeared as regions of high probability within the joint distribution of $X(t)$ and $X_H(t)$.

In Fig. S5 we display higher magnification joint probability distributions corresponding to those illustrated in the main text.

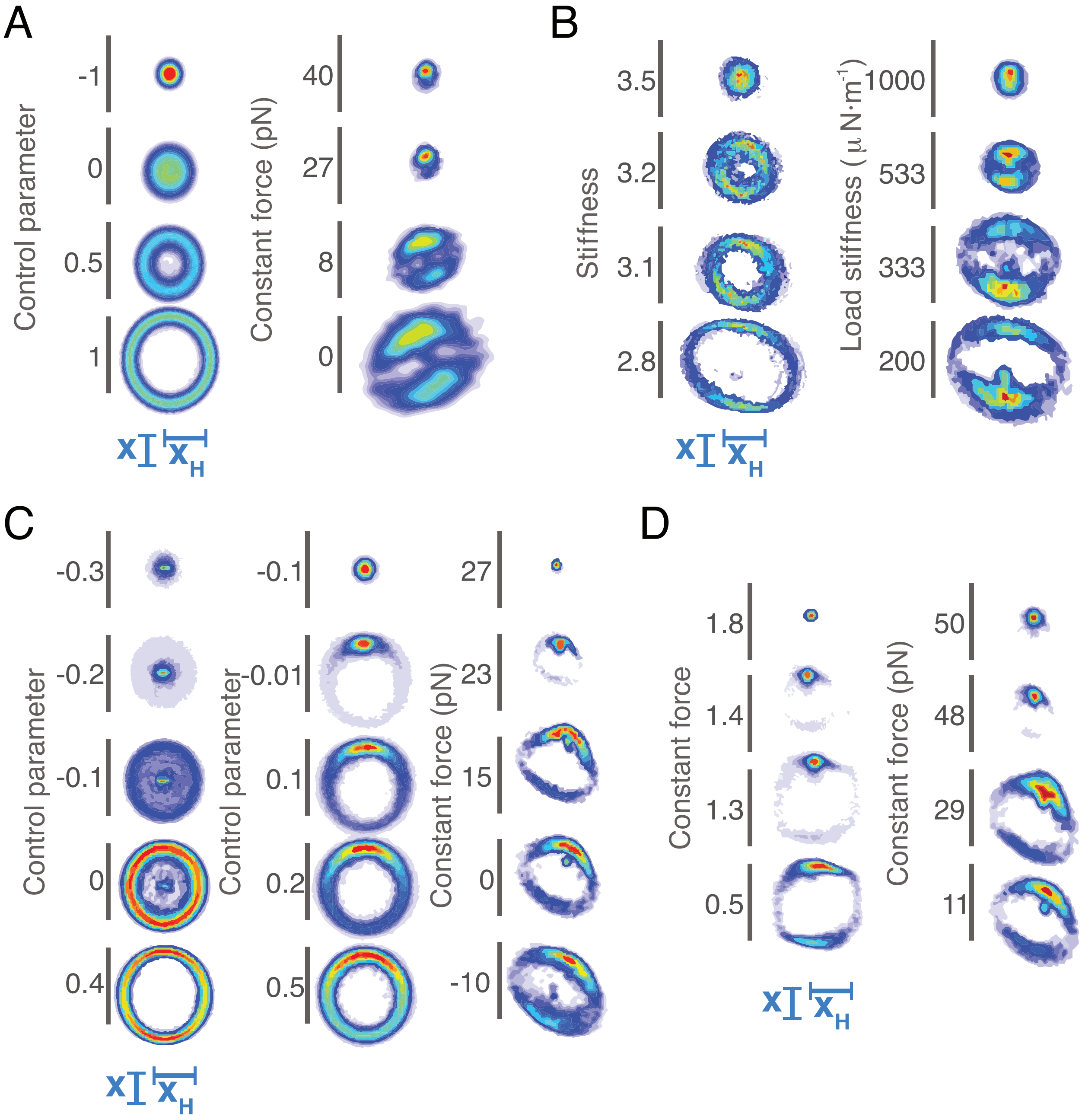

Figure S5: **Analytic distributions from a system's analytic signal.** For the distributions displayed in Fig. 2 (A), Fig. 3 (B), Fig. 4 (C), and Fig. 5 (D), we show the joint probability distributions of each system's position X and the Hilbert transform of its position X_H. The data in each column are presented in the same order as those in the associated figures.

C.3 Peak Detection

Using a peak-detection algorithm [7], we defined for each time series the local maxima and minima as respectively peaks and troughs in the signal. For a given threshold δ, peaks and troughs were defined as

$$P_j = \max_X \left\{ X\colon X\epsilon \left\{ P_i\colon t_{T_j} \leq t_{P_i} \leq t_{T_{j+1}} \right\} ; T_j + \delta \leq X \cap T_{j+1} + \delta \leq X \right\} , \tag{S14}$$

$$T_j = \min_X \left\{ X\colon X\epsilon \left\{ T_i\colon t_{P_j} \leq t_{T_i} \leq t_{P_{j+1}} \right\} ; P_j - \delta \geq X \cap P_{j+1} - \delta \geq X \right\} , \tag{S15}$$

in which P_j and T_j correspond respectively to the j^{th} peak or trough in the signal and t_{P_j} and t_{T_j} are the times at which the j^{th} peak or trough occurs. We specified a number of thresholds that fell between the maximum noise floor and the maximum amplitude of oscillation from the time series across all operating points.

C.4 Amplitude from Peak Detection

We defined the peak-to-peak magnitude as the difference between the value of each peak P_j and the nearest trough. For each time series, we reported the mean amplitude as one-half the mean peak-to-peak magnitude. The associated error bars represented the standard errors of the mean from five time series for stochastic simulations and the standard error from 10^4 bootstrapped samples for experimental results.

C.5 Frequency from Peak Detection

We calculated the mean frequency of oscillation $\langle r \rangle$ for each time series as the inverse of the mean inter-event interval $\langle IEI \rangle$

$$\langle r \rangle = \frac{1}{\langle IEI \rangle}, \tag{S16}$$

in which the inter-event interval corresponds to the length of time between successive peaks, $IEI_k = t_{P_{k+1}} - t_{P_k}$. The mean frequency can additionally be estimated as the number of peaks $n(P)$ divided by the length of the signal in time T:

$$\langle r \rangle = \frac{n(P)}{T}. \tag{S17}$$

In this study, we reported the frequency calculated from Equation S16 and confirmed that these values accorded with those from Equation S17. For stochastic simulations, error bars represented the standard errors of the mean from five time series. For hair-bundle data, error bars represented standard errors calculated from 10^4 bootstrapped samples.

C.6 Coefficient of Variation from Peak Detection

To assess the regularity of oscillations in a time series, we calculated the coefficient of variation C_V for the distribution of inter-event intervals

$$C_V = \frac{\sqrt{\langle \Delta IEI^2 \rangle}}{\langle IEI \rangle}, \tag{S18}$$

in which $\left\langle \Delta IEI^2 \right\rangle = \left\langle IEI^2 \right\rangle - \left\langle IEI \right\rangle^2$ represents the variance of IEI and $\sqrt{\langle \Delta IEI^2 \rangle}$ its standard deviation. The coefficient of variation is larger for irregular oscillations than it is for regular ones. We estimated the control parameter at which a bifurcation occurred as the value for which C_V crossed an empirically derived threshold. To distinguish limit-cycle oscillation from stochastic switching between stable states, we selected a threshold of 0.5 because the coefficient of variation is never less than 0.5 in the case of stochastic switching (Section D.6). Error bars represented the standard errors of the mean from five time series for stochastic simulations and standard errors from 10^4 bootstrapped samples for experimental data. In many cases we excluded from display coefficients of variation drawn from a pool of fewer than 0.05 counts per unit time (*e.g.* three counts for a 60-second time series of bundle motion or 100 counts for a numerical simulation with 10^4 units of time).

C.7 Fourier Transform

We estimated the amplitude and frequency of spontaneous oscillation from a noisy system's Fourier transform. With a moderate level of noise ($\sigma_R = \sigma_I = 0.1$, see Section D), the estimates for each time series revealed patterns consistent with those expected for a system operating near the relevant bifurcation (Fig. S6). Near a supercritical Hopf bifurcation, the amplitude rose gradually with an increase in the control parameter and the frequency of oscillation remained constant when that parameter exceeded zero (Fig. S6A). Near a SNIC bifurcation, the frequency of oscillation grew gradually from zero as the control parameter increased and the amplitude of oscillation rose sharply until it achieved a nearly constant value (Fig. S6B). Finally, a system operating near a subcritical Hopf bifurcation possessed an amplitude and frequency that both rose sharply near the associated saddle-node of limit cycles bifurcation and gradually increased thereafter (Fig. S6C). These examples show that the Fourier transform can be used to estimate the location of a bifurcation if the noise level is low.

To demonstrate that the Fourier transform of a time series may fail to evidence the presence of a bifurcation when the noise level is large, we calculated the amplitude and frequency of spontaneous oscillation from stochastic simulations of a model of hair-bundle dynamics (see Section E). Here the amplitude and frequency of oscillation failed to indicate the transection of either a subcritical or a supercritical Hopf bifurcation (Fig. S7). In spite of the fact that this simulation involved long time series ($5 \cdot 10^8$ points) and several spectra we averaged to improve the signal-to-noise ratio, the results remained poor.

We next determined that the Fourier transform of a hair bundle's time series was less successful at indicating the onset of oscillations than the peak-detection algorithm. We defined the amplitude and frequency from the peak of maximal height in the bundle's amplitude spectrum (Fig. S8A). In many cases, however, the spectrum displayed multiple peaks of similar height. The presence of more than one peak made it difficult to select an appropriate maximum, which in turn yielded a poor estimate of the frequency of spontaneous oscillation.

In response to a decrease in constant force, the peak-detection algorithm yielded a sharp rise to a nearly constant amplitude of oscillation indicating the onset of oscillations near a bifurcation and a gradual growth in frequency for both peak-detection thresholds (Fig. S8B). The amplitude and frequency estimated from the Fourier transform displayed large fluctuations obscuring the onset of oscillations (Fig. S8C). The bundle's amplitude of spontaneous oscillation calculated from the Fourier transform was sometimes only about half that computed from the peak-detection algorithm.

When a hair bundle displays spikes, calculation of its amplitude and frequency of spiking from the peak-detection algorithm yields more accurate results than those from its spectra (Fig. S9). To demonstrate this, we calculated the amplitude and frequency of spiking for a model hair bundle. The bundle displayed spikes with an amplitude exceeding one and a frequency of approximately 0.01 (Fig. S9A). The bundle's spectrum displayed a broad peak (Fig. S9B). Subdividing the signal into increasing numbers of non-overlapping windows to calculate averaged spectra made this peak clearer, but the peak remained broad. We then calculated for increasing numbers of non-overlapping windows the amplitude and frequency of spiking using both the peak-detection algorithm and the bundle's spectra. As the number of windows used for averaging increased, the amplitude of spiking calculated using three different peak-detection thresholds remained constant around 1.7-1.75 (Fig. S9C). However, the amplitude calculated from the averaged spectra increased from 0.04 to a maximum of 0.18 as the number of windows increased. The amplitude of spiking calculated using the bundle's averaged spectra therefore yielded a result that did not agree with the expected amplitude from the raw time series (Figure S9A). The frequency of spiking calculated using the peak-detection algorithm also remained constant around 0.01 as the number of windows changed (Fig. S9D). This value agrees with the expected frequency of 0.01 from the raw time series (Fig. S9A). However, the frequency of spiking calculated using the bundle's averaged spectra fluctuated greatly around 0.02-0.03 as the number of windows changed, well above the expected spiking frequency. Furthermore, there was no obvious improvement in the estimate of the bundle's frequency of spiking using its averaged spectra as the number of windows increased. The peak-detection algorithm therefore performed better than spectral analysis in capturing the amplitude and frequency of spiking. Because the peak-detection algorithm produced accurate estimates of spike amplitudes and rates and indicated the onset of oscillations, we employed this method throughout this study.

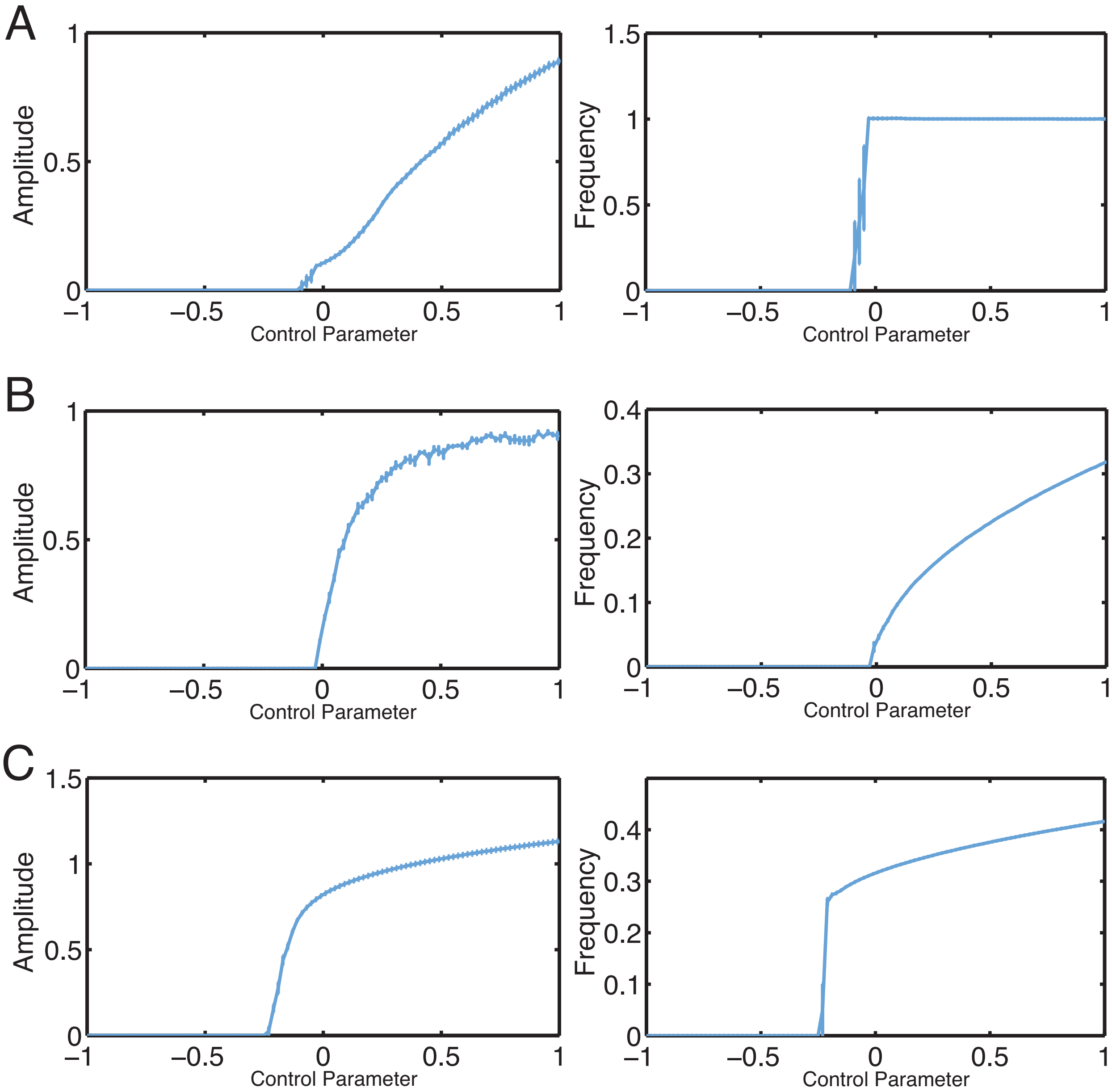

Figure S6: **Amplitude and frequency of oscillation for noisy systems near different bifurcations.** We calculated the amplitude (left column) and frequency (right column) of oscillation as the peak in the Fourier transform of a time series. (A) For a system described by the normal form of a supercritical Hopf bifurcation, the amplitude rose gradually with the control parameter and the frequency remained constant on the oscillatory side of the bifurcation. (B) A system crossing a SNIC bifurcation exhibited an oscillation amplitude that asymptoted to a constant value as the control parameter increased. With a decrease in the control parameter, its frequency of oscillation fell to an arbitrarily small value. (C) For a system described by the normal form of a subcritical Hopf bifurcation, the amplitude and frequency both increased sharply on the non-oscillatory side of the deterministic bifurcation and subsequently grew gradually as the control parameter continued to rise. All simulations were integrated numerically as described in Section D with noise levels of $\sigma_R = \sigma_I = 0.1$. Error bars correspond to the standard errors of the mean from five time series.

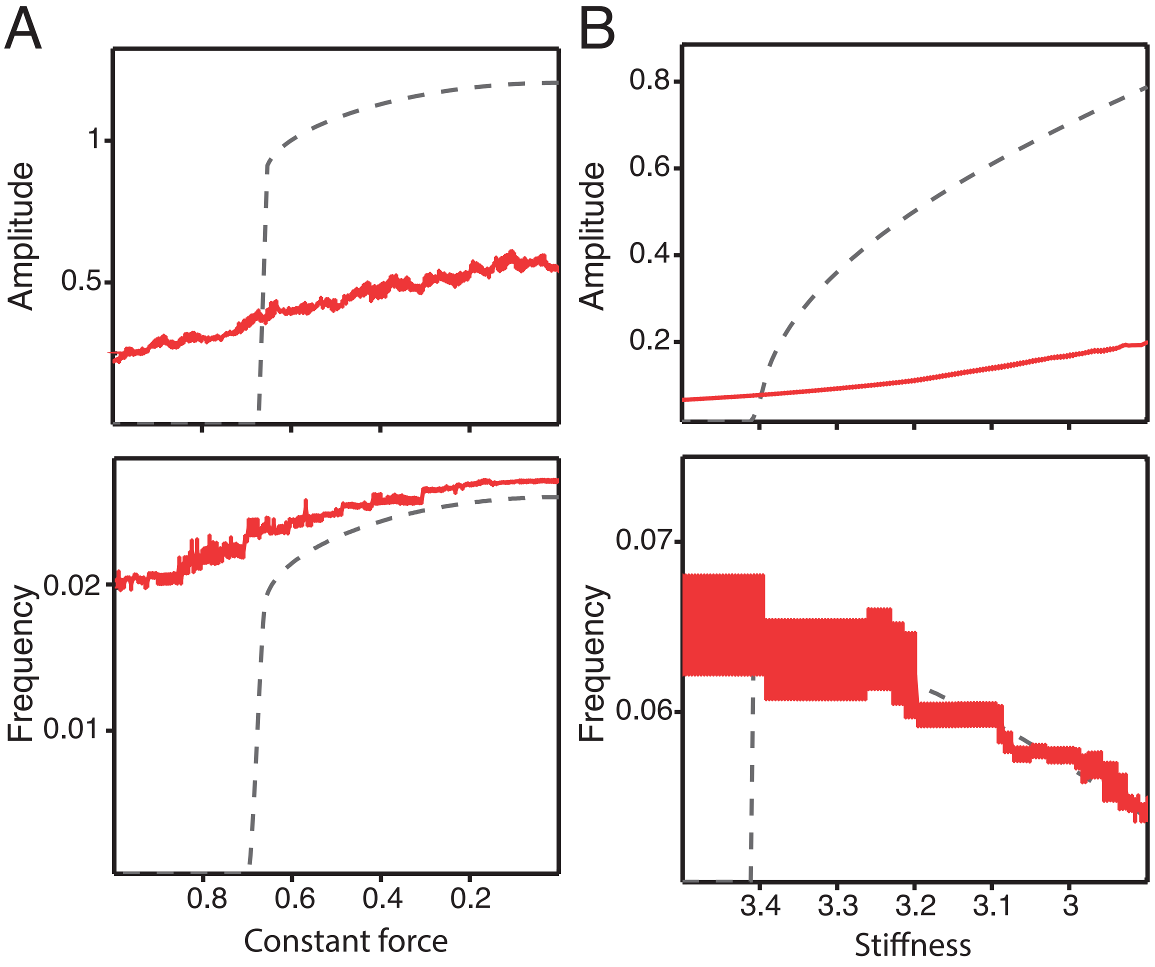

Figure S7: **Amplitude and frequency of oscillation for a model hair bundle in the presence of noise.** We calculated the amplitude (top) and frequency (bottom) of oscillation as the peak in the Fourier transform of a time series. (A) For a stiffness of 2, a model hair bundle crossed a subcritical Hopf bifurcation with changes in constant force. In the absence of noise, both the amplitude and frequency of oscillation rose sharply near the bifurcation, then gradually on the oscillatory side of the bifurcation with decreases in constant force (dashed line). In the presence of noise, neither the amplitude nor the frequency indicated a bifurcation had been transected and the amplitude fell to less than half the value obtained in the noise-free scenario (red). (B) At a constant force of 0, the model bundle crossed a supercritical Hopf bifurcation with an increase in stiffness. In the absence of noise the amplitude rose gradually from zero and the frequency achieved a non-zero value at the bifurcation before falling with further decreases in load stiffness (dashed line). The addition of noise effaced the transition from zero to non-zero in amplitude, which for the largest amplitudes fell to less than one-fifth the value of the noise-free scenario (red). The pattern in amplitude was qualitatively similar to that of the subcritical Hopf bifurcation. Noise eliminates some differences between supercritical and subcritical Hopf bifurcations. All panels correspond to numerical simulations of a model of hair-bundle dynamics as outlined in Section E with a noise level of $\sigma_X = \sigma_f = 0.2$. Error bars correspond to the standard errors of the mean from five time series.

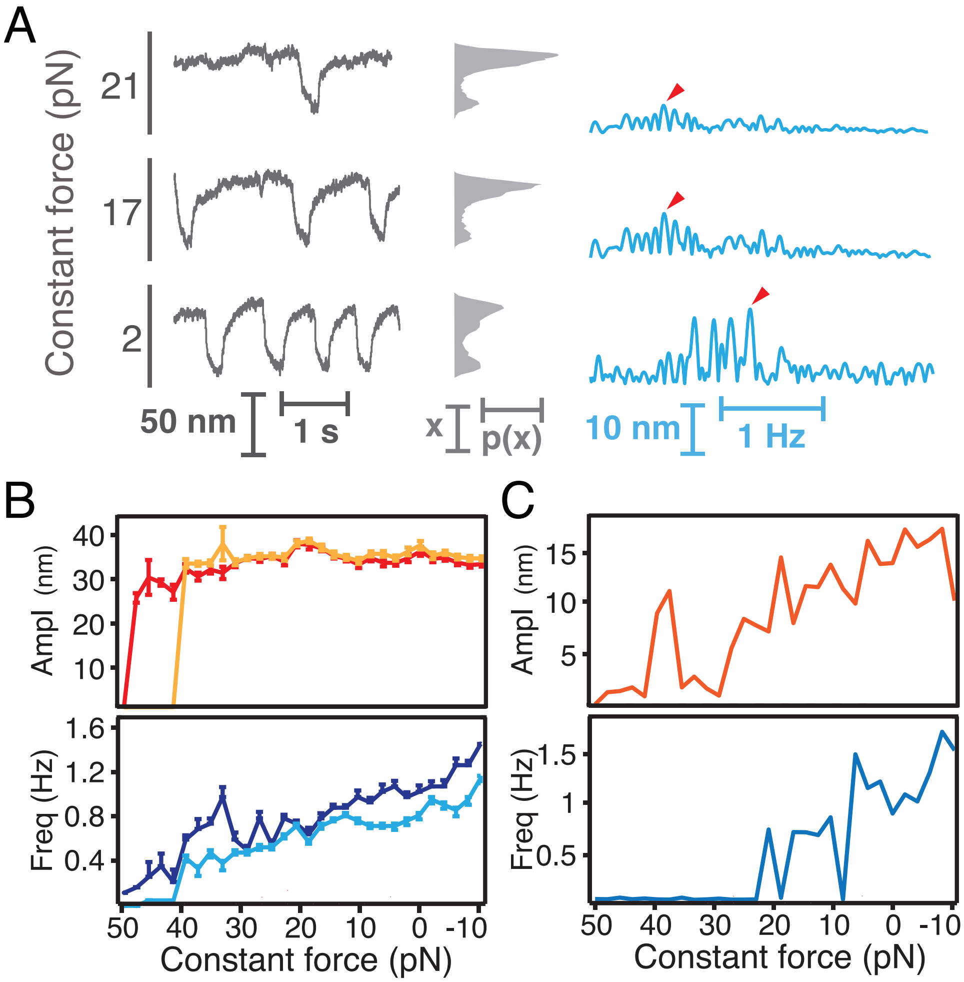

Figure S8: **Comparison of amplitude and frequency calculations for experimental data.** (A) Displayed on the left are the time series and position histograms for the bundle in Fig. 5. We calculated the amplitude and frequency of oscillation from the peak (red arrowhead) in the bundle's spectrum (blue, right). (B) We calculated with a peak-detection algorithm the bundle's amplitude (red, orange) and frequency (dark and light blue) of spontaneous oscillation. We used thresholds of 50 nm (red, dark blue) and 60 nm (orange, light blue). (C) We compared the results in panel B with the amplitude and frequency curves calculated from the bundle's Fourier transform. For all panels, the load stiffness was 100 $\mu\mathrm{N} \cdot \mathrm{m}^{-1}$ and the proportional gain was 0.1. We used a stimulus fiber with a stiffness of 139 $\mu\mathrm{N} \cdot \mathrm{m}^{-1}$ and a drag coefficient of 239 $\mathrm{nN} \cdot \mathrm{s} \cdot \mathrm{m}^{-1}$. Additional analyses can be found in Figs. 5H-N. Error bars represent standard errors of the means from 10^4 bootstrap samples. To detect a peak in the spectrum with accuracy the time series must be sufficiently long to produce the required frequency resolution. Because of this requirement the time series was not partitioned into windows for averaging.

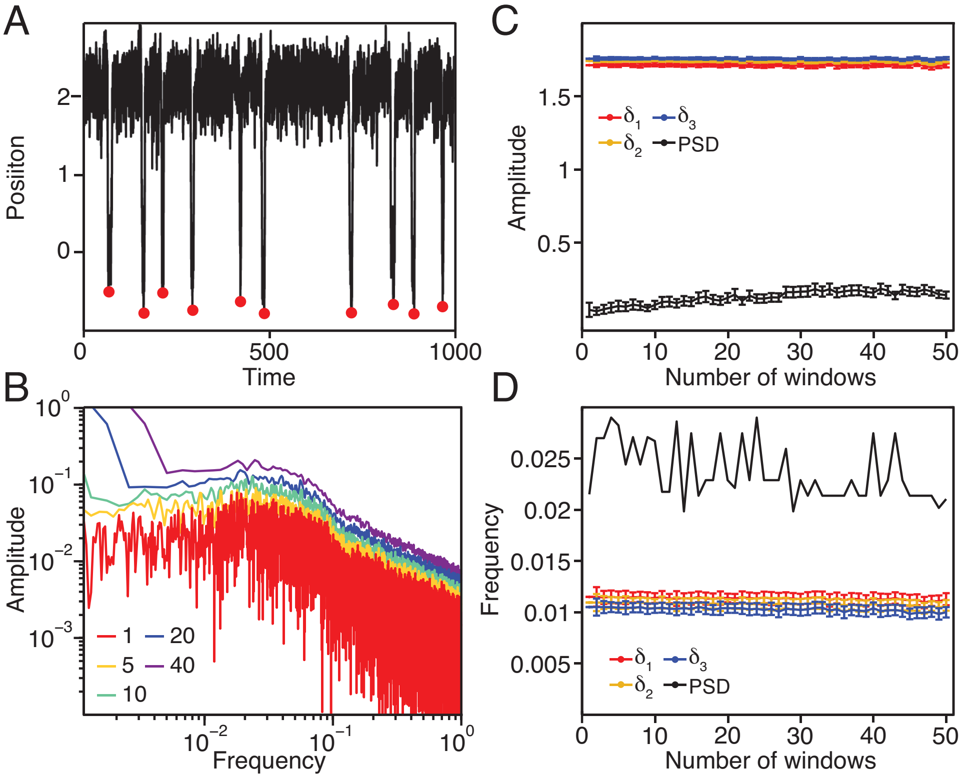

Figure S9: **Comparison of amplitude and frequency calculations for simulated data.** (A) A model bundle subjected to a constant force of 2 and a stiffness of 2 displayed large-amplitude spikes. The peak-detection algorithm successfully identified each spike for a peak-detection threshold of 3 (red circles). Over the course of this time segment, the bundle displayed approximately 0.01 spikes per time point with an amplitude larger than one. (B) Spectra for the entire time series of $2 \cdot 10^6$ time points are displayed for different numbers of non-overlapping windows, in which each spectrum is an average over the number of windows indicated (red through purple). (C) The bundle's spike amplitude was calculated using both a peak-detection algorithm with three thresholds and the averaged spectra for one through fifty non-overlapping time windows. The amplitude remained constant around 1.7-1.75 for all peak-detection thresholds ($\delta_1 = 2$, $\delta_2 = 2.5$, $\delta_3 = 3$) as the number of non-overlapping windows increased from one to fifty. However, the amplitude calculated from the peak in the bundle's averaged spectrum increased from 0.04 to a maximum of 0.18 as the number of windows increased. (D) The bundle's frequency of spiking was calculated using the same method in (C). The frequency of spiking remained constant around 0.01-0.011 for all peak-detection thresholds as the number of windows increased. However, the frequency of spiking calculated using the bundle's averaged spectra displayed large fluctuations from 0.02-0.03 as the number of windows changed from 1-48. When the number of windows became 49 or larger, the averaged spectra possessed too few points to accurately determine the position of the peak. All spectra were calculated using Welch's method. Simulations were performed in MATLAB using equations S31-S32 and a noise level of 0.4. Error bars represent standard errors of the means for the number of averages shown on the abscissa.

C.8 Analytic Information

A system that exhibits limit-cycle oscillations in a two-dimensional phase space displays a high degree of correlation between the two relevant dimensions. A system dominated by noise, however, evidences less correlation between these variables. We therefore sought to estimate the onset of limit-cycle oscillations by measuring the analytic information, which is the mutual information between the real and imaginary parts of a system's analytic signal. As described in Section C.2, we generated an analytic distribution from a system's real-valued signal X and its Hilbert transform X_H. We then calculated the mutual information between X and X_H as

$$I(X;X_H) = \sum_{i=1}^{L_X} \sum_{j=1}^{L_{X_H}} p(i,j) \cdot \log_2 \left(\frac{p(i,j)}{p(i) \cdot q(j)} \right), \tag{S19}$$

in which $p(i,j)$ is height of the bin with index $\{i,j\}$ for the histogram estimating the joint probability distribution between X and X_H and $p(i)$ and $q(j)$ are respectively the values of the marginal probability distributions of X at index i and of X_H at index j. L_X and L_{X_H} correspond respectively to the number of bins used to estimate the distributions for X and X_H. We calculated the analytic information in this manner over 2^8-2^{11} equal-width bins in the analytic distribution, employing the same number of bins for all time series in a given experiment or simulation. Using this metric, we found that the analytic information rose with the emergence of limit-cycle oscillations (Figs. 2-5). For narrow-band Gaussian noise, the analytic information instead approached zero as the length of the sequence of randomly-generated outcomes increased (Fig. S10).

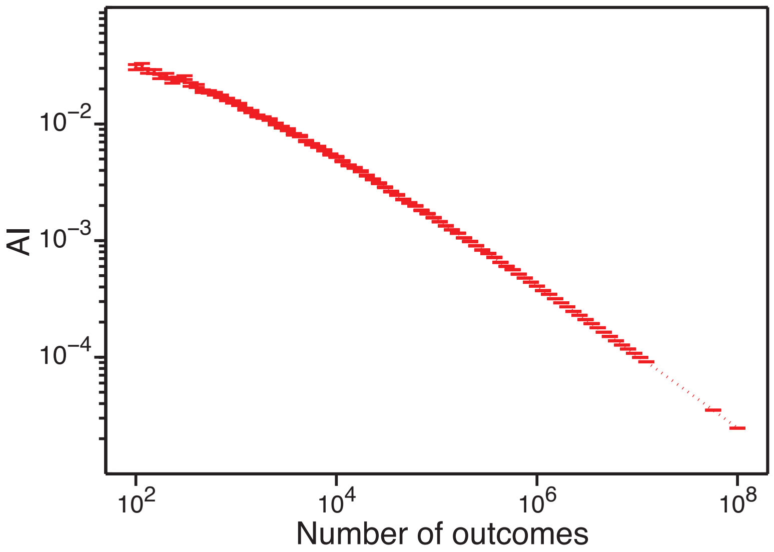

Figure S10: **Analytic information of narrow-band Gaussian noise as a function of the number of outcomes.** We calculated the analytic information for narrow-band Gaussian noise for increasing numbers of outcomes. As the number of outcomes increased by one millionfold, the analytic information fell by more than one thousandfold. All calculations of analytic information employed 2^8 equal-width bins. Error bars represent the standard errors of the mean for 100 repetitions.

SECTION D

Noisy Simulations of Bifurcation Normal Forms

In order to identify and locate different bifurcations in the presence of noise, we employed the metrics from Section C to noisy time series drawn from systems operating near different bifurcations. Each of these noisy systems can be described by a simple mathematical object—a normal form—that captures the generic features of a particular bifurcation. By employing the same metrics to both our simulations and our experiments, we could then compare these results to identify and locate the bifurcations near which hair bundles might operate.

We performed stochastic simulations of the normal forms of various bifurcations. All equations were numerically integrated with the Euler-Murayama method in MATLAB (R2014a). For each normal form we simulated time series across 500 values of the control parameter ranging from -5 to 5. Each time series possessed $5 \cdot 10^7$ points and was subsequently divided into five partitions of 10^7 points apiece to obtain five examples at each operating point. Each simulation incorporated white noise with standard deviations of 0.05, 0.1, 0.2, and 0.4.

D.1 Supercritical Hopf Bifurcation

Simulations of the supercritical Hopf bifurcation employed the two coupled planar equations

$$dX_R = \left[\mu X_R - \omega X_I - X_R \cdot (X_R^2 + X_I^2)\right] \cdot dt + \sigma_R \cdot dW_R, \tag{S20}$$

$$dX_I = \left[\omega X_R + \mu X_I - X_I \cdot (X_R^2 + X_I^2)\right] \cdot dt + \sigma_I \cdot dW_I, \tag{S21}$$

in which μ is a control parameter, ω is an angular frequency, and X_R and X_I are respectively the real and imaginary parts of the signal. Here W_R and W_I are Wiener processes, such that $\sigma_R \cdot dW_R$ and $\sigma_I \cdot dW_I$ are normally distributed white-noise increments with standard deviations of σ_R and σ_I. For our simulations we defined $\omega = 2\pi$. A supercritical Hopf bifurcation occurs at $\mu = 0$, birthing limit-cycle oscillations for $\mu > 0$. We therefore define $\mu < 0$ and $\mu > 0$ as respectively the quiescent and oscillatory sides of the deterministic Hopf bifurcation.

D.2 Subcritical Hopf Bifurcation

Simulations of the subcritical Hopf bifurcation employed the two coupled planar equations

$$dX_R = \left[\mu X_R - \omega X_I + X_R \cdot (X_R^2 + X_I^2) - X_R \cdot (X_R^2 + X_I^2)^2\right] \cdot dt + \sigma_R \cdot dW_R, \tag{S22}$$

$$dX_I = \left[\omega X_R + \mu X_I + X_I \cdot (X_R^2 + X_I^2) - X_I \cdot (X_R^2 + X_I^2)^2\right] \cdot dt + \sigma_I \cdot dW_I, \tag{S23}$$

in which μ is a control parameter, ω is a frequency, and the noise terms are the same as those for the supercritical Hopf bifurcation. We defined $\omega = 2\pi$ for all stochastic simulations. The subcritical Hopf bifurcation occurs at $\mu = 0$ and a saddle-node of limit cycles bifurcation resides at $\mu = -0.25$. We again define $\mu > 0$ as the oscillatory side of the deterministic Hopf bifurcation. There is a quiescent region near the subcritical Hopf bifurcation defined by $\mu < -0.25$, as there is coexistence of a limit cycle with a stable fixed point for $-0.25 < \mu < 0$.

D.3 Saddle-Node on Invariant Cycle (SNIC) Bifurcation

A system operating near a SNIC bifurcation may be defined in polar coordinates [16, 17, 18]:

$$\dot{r} = r \cdot (1 - r^2), \tag{S24}$$

$$\dot{\theta} = 1 - \cos\theta + \mu \cdot (1 + \cos\theta), \tag{S25}$$

in which r and θ describe motion in respectively the radial and angular directions. Strictly speaking, Equation S25 is the normal form of the SNIC bifurcation, and Equation S24 is an auxiliary equation that is necessary to define the amplitude dynamics. A SNIC bifurcation occurs at $\mu = 0$, with limit-cycle oscillations existing for all values of μ exceeding zero. We performed a change of variables to describe this system using the two coupled planar equations

$$dX_R = \left\{(1 - X_R^2 - X_I^2) \cdot X_R - X_I \cdot \left[1 - \frac{X_R}{\sqrt{X_R^2 + X_I^2}} + \mu \cdot \left(1 + \frac{X_R}{\sqrt{X_R^2 + X_I^2}}\right)\right]\right\} \cdot dt + \sigma_R \cdot dW_R, \tag{S26}$$

$$dX_I = \left\{(1 - X_R^2 - X_I^2) \cdot X_I + X_R \cdot \left[1 - \frac{X_R}{\sqrt{X_R^2 + X_I^2}} + \mu \cdot \left(1 + \frac{X_R}{\sqrt{X_R^2 + X_I^2}}\right)\right]\right\} \cdot dt + \sigma_I \cdot dW_I, \tag{S27}$$

in which all noise terms are defined in the same manner as those for a Hopf bifurcation. We define the quiescent and oscillatory sides of the deterministic bifurcation as respectively $\mu < 0$ and $\mu > 0$.

D.4 Saddle-Node Bifurcation

We additionally performed stochastic simulations of a system crossing a saddle-node bifurcation. To do so, we employed the normal form of a cusp bifurcation, given by [19]:

$$dX = \left[\mu + bX - X^3\right] \cdot dt + \sigma \cdot dW, \tag{S28}$$

in which μ and b are control parameters. We used $b = 0.2565$, so that a saddle-node bifurcation occurs at $\mu = \mp\frac{2}{3\sqrt{3}}b^{3/2} \approx \mp 0.05$. Simulations were obtained over 500 values of μ ranging from -0.5 to 0, each with $5 \cdot 10^8$ points and subsequently divided into five time series with 10^8 points apiece, one order of magnitude longer than the simulations described in Sections D.1-D.3.

D.5 Frequency of Motion in the Presence of Noise

We performed stochastic simulations of each of the normal forms outlined in Sections D.1-D.4. To assess the dependence of our calculations on the level of noise, we compared the relationship between frequency and control parameter at two noise levels, for which $\sigma = \sigma_R = \sigma_I$, and two peak-detection thresholds for each normal form (Fig. S11).

A system operating near a supercritical Hopf bifurcation should exhibit a discontinuous jump in frequency to a non-zero value upon crossing the bifurcation (Fig. S11A). However, the addition of noise blurred this discontinuity, resulting in a gradual rise in the frequency of oscillation to a constant value at $\mu > 0$. Increasing the value of the peak-detection threshold shifted the frequency curve rightward. A system operating in the vicinity of a subcritical Hopf bifurcation instead exhibited limit-cycle oscillations in the coexistence and quiescent regions near the deterministic bifurcation ($\mu < 0$) in the presence of noise (Fig. S11B). Although noise blurred the sharp rise in frequency predicted in a deterministic scenario, the subcritical Hopf bifurcation could be distinguished from its supercritical counterpart for sufficiently weak noise by a peak-detection algorithm. For the subcritical Hopf bifurcation an increase in the peak-detection threshold did not shift the curve rightward at low noise levels. However, when the noise was large ($\sigma = 0.2$) the shift reappeared rendering the subcritical Hopf similar to a supercritical Hopf bifurcation, as the oscillation frequency asymptotes to a constant as the control parameter is increased in both cases.

A system crossing a SNIC bifurcation displayed a frequency that rose gradually from zero in the absence of noise (Fig. S11C). Adding noise caused the system to cross a separatrix in its phase space, inducing all-or-none excursions with a frequency that depended on the noise level. Unlike the frequency relationship for a supercritical Hopf bifurcation, that of a SNIC bifurcation was insensitive to changes in the peak-detection threshold.

Finally, a system crossing a saddle-node bifurcation displayed a frequency that depended strongly on both the noise level and the peak-detection threshold (Fig. S11D). When the noise level was larger or the peak-detection threshold smaller, the detected frequency of motion increased for all operating points and achieved a maximum at $\mu = 0$. Unlike the previous bifurcations, the frequencies for different noise levels and peak-detection thresholds did not converge to the same values when the control parameter became large. For a deterministic system, in which the noise level was zero, no peaks were detected and the frequency was zero (not shown).

D.6 Irregularity of Interpeak Intervals in a Bistable System

A bistable system displays noise-induced switching between its stable states, revealing a bimodal distribution of positions. Because the switching arises from noise-induced motion, however, we expect the residence times to be irregular. In such a scenario, the distribution of interpeak intervals will be broad and the coefficient of variation large. The coefficient of variation does not distinguish between the monostable and bistable sides of a saddle-node bifurcation (Fig. S12). The dip statistic rises, however, as a system transitions from monostability to bistability.

Stochastic switching between states A and B of a double-well potential can be idealized by homogeneous Poisson processes between the two states. The distribution of durations for which the particle remains in either state A or state B—the residence-time distribution—is therefore exponential. When calculating the coefficient of variation we quantified the time between peaks in a time series, which represents the time for a particle to start in state B (or A) and to return to state B (or A). Let the time τ between events represent the time between starting in state B and returning to state B. The distribution of τ follows

$$P(\tau) = N \cdot \int_{0}^{\tau} \lambda_1 \exp\left(-\lambda_1 t\right) \lambda_2 \exp\left(-\lambda_2 (\tau - t)\right) dt, \tag{S29}$$

in which N is a normalization constant, and λ_1 is the rate at which the system transitions from B to A and λ_2 is the rate of transitioning from A to B. The coefficient of variation for this distribution is

$$C_V = \frac{\sqrt{\lambda_1^2 + \lambda_2^2}}{\lambda_1 + \lambda_2}. \tag{S30}$$

In the case that $\lambda_1 = \lambda_2$, the coefficient of variation becomes $C_V = 1/\sqrt{2} \approx 0.7$. When either $\lambda_1 \to \infty$ or $\lambda_2 \to \infty$, the coefficient of variation instead becomes $C_V = 1$, which is what we expect for an exponential distribution. Consequently, a noisy, bistable system's coefficient of variation never falls below 0.7. To rule out bistability in experimental observations, we choose a threshold for the coefficient of variation of 0.5. This conservative threshold allows us to account for numerical errors that could allow the coefficient calculated for a bistable system to attain values slightly below 0.7 (Fig. S12). The variance in the recurrence time is smaller in the two-state Poisson process limit than it is for a system with multiple stable states. The coefficient of variation for a multistable system therefore always exceeds $1/\sqrt{2}$. This threshold on the coefficient of variation therefore distinguishes a system's operation in a bistable or multistable regime from operation in a regime allowing limit-cycle oscillations.

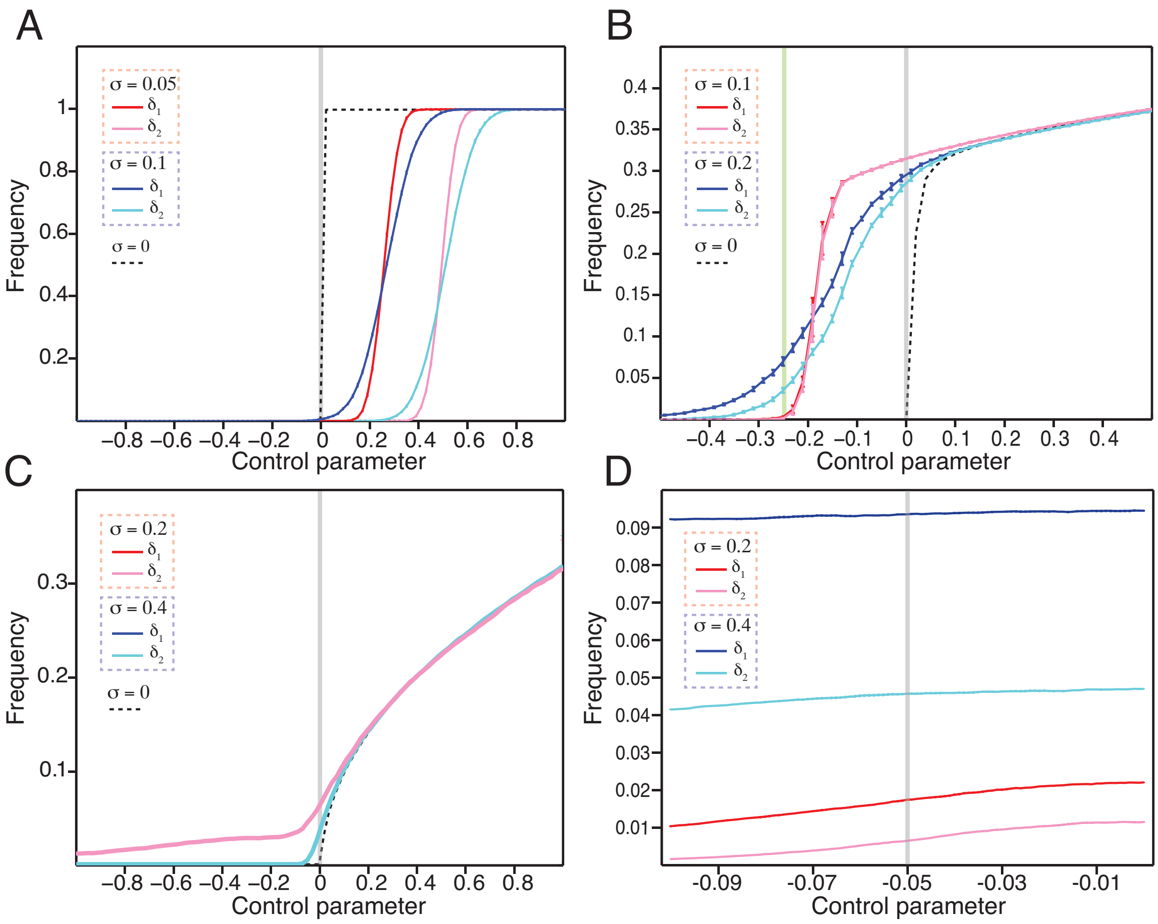

Figure S11: **Dependence of the frequency of oscillation on noise level.** (A) Simulations of the normal form of a supercritical Hopf bifurcation reveal changes in the frequency of oscillation with variation of the control parameter. Here the bifurcation resides at $\mu = 0$ (gray line). In the absence of noise, the spike rate discontinuously jumped to a non-zero value and remained constant upon crossing the bifurcation (dashed line). Adding noise caused the slope of this relationship to decrease as a function of the noise level (red *vs.* blue). Changing the peak-detection threshold at a given level of noise shifted the frequency relationship without changing its slope (red *vs.* pink). (B) A subcritical Hopf bifurcation resides at $\mu = 0$ (gray line) and a saddle-node of limit cycles at $\mu =$ -0.25 (green line). In the absence of noise with initial conditions $X_R = X_I \approx 0$, the spike rate rose discontinuously upon crossing the Hopf bifurcation and slowly increased until it achieved a constant value for $\mu \gg 0$. Adding noise caused limit-cycle oscillations to appear in the coexistence and quiescent regions near the deterministic bifurcation ($\mu < 0$). With a low noise level, the spike rate curve had a similar shape as in the deterministic case and fell to zero near the saddle-node of limit cycles (red and pink). Higher noise levels skewed the curve and induced ringing in the quiescent regime (blue and cyan). Changing the threshold yielded either little change in the spike rate relationship (red *vs.* pink) or a small change in its slope and magnitude near the bifurcation (blue *vs.* cyan). (C) A SNIC bifurcation occurs at $\mu = 0$ (gray line). Oscillations emerged with an arbitrarily low frequency at $\mu = 0$ and grew in frequency as μ increased. Adding noise increased the frequency near the bifurcation and induced oscillations for $\mu < 0$. Changing the peak-detection threshold caused no change in this relationship. (D) A saddle-node bifurcation occurs near $\mu =$ -0.05. Increasing the noise level or decreasing the peak-detection threshold increased the fluctuation frequency across all operating points. For panels A-C, we employed thresholds of $\delta_1 = 1$ and $\delta_2 = 1.5$. Panel D employed thresholds of $\delta_1 = 0.8$ and $\delta_2 = 1.2$. Deterministic plots were calculated with a threshold of 10^{-3}. Error bars represent standard errors of the means for five time series.

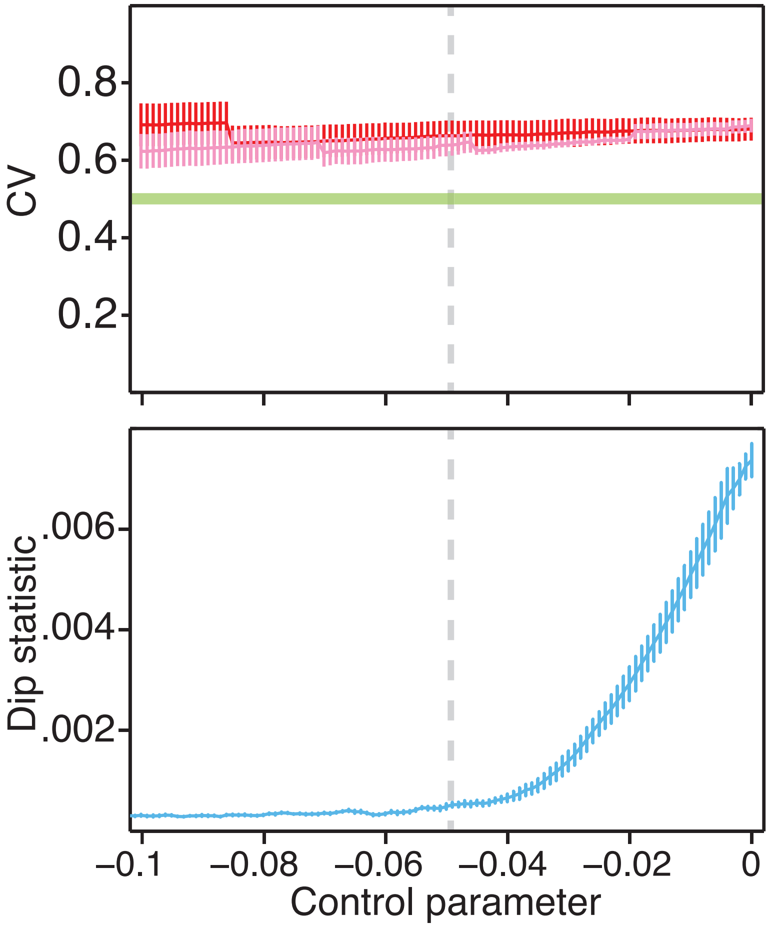

Figure S12: **Coefficient of variation and dip statistic for a system possessing both monostable and bistable regimes.** A system is monostable for control-parameter values below -0.05 and bistable for values above this threshold, at which a saddle-node bifurcation occurs. (Top) For a noisy system crossing a saddle-node bifurcation, the coefficients of variation remained larger than a threshold of 0.5 (green line) for peak-detection thresholds of $\delta_1 = 0.8$ (red) and $\delta_2 = 1.2$ (pink) and a noise level of $\sigma = 0.4$. (Bottom) At the same noise level, the system displays a rise in its dip statistic after crossing the saddle-node bifurcation. Gray dashed lines correspond to the saddle-node bifurcation's location. Error bars represent standard errors of the mean for five repetitions.

SECTION E

Noisy Simulations of a Model of Hair-Bundle Mechanics

We next wished to compare the behavior of experimentally observed hair bundles to simulated ones whose operation near a particular bifurcation is known. This allowed us to test the metrics in Section C on a noisy system that possesses both the generic features of particular bifurcations and behaviors specific to hair bundles. In doing so, we could further verify our ability to identify and locate bifurcations near which noisy bundles might operate.

We performed stochastic simulations of a model of hair-bundle dynamics by the method outlined in Section D. Each time series contained $5 \cdot 10^8$ points and was divided into five partitions of 10^8 points apiece to obtain five examples at each of 500 operating points. Each simulation incorporated white noise generated by the Mersenne twister pseudorandom-number generator with standard deviations of 0.05, 0.1, 0.2, 0.4, 0.5, and 1. We repeated the simulations for a constant force of 0 with stiffnesses ranging from 0 through 4 and for load stiffnesses of 1.5, 1.75, 2, 2.5, and 3 with constant forces ranging from 0 through 2.

E.1 Mathematical Description

The following description captures the dynamics of a mechanically loaded hair bundle [2, 3]:

$$dX = \left[a \cdot (X - f) - (X - f)^3 - K_T \cdot X + F_C\right] \cdot dt + \sigma_X \cdot dW_X, \tag{S31}$$

$$df = \frac{1}{\tau_f} (b \cdot X - f) \cdot dt + \sigma_f \cdot dW_f, \tag{S32}$$

in which X is the bundle's position, f is the force owing to adaptation, a is stiffness owing to gating of the mechanotransduction channel, τ_f is the timescale of adaptation, and b is a stiffness coupling bundle position to adaptation. The total stiffness of the bundle with a mechanical load is $K_T = K_B + K_L$, in which K_B is the bundle's stiffness and K_L is that of its load. The bundle may also be subjected to a constant force F_C. W_X and W_f are Wiener processes such that $\sigma_X \cdot dW_X$ and $\sigma_f \cdot dW_f$ are normally distributed white-noise increments with standard deviations of σ_X and σ_f. For all simulations, we used $\sigma = \sigma_X = \sigma_f$, $a = 3.5$, $b = 0.5$, and $\tau_f = 10$.

E.2 Analysis of a Model Hair Bundle in the Presence of Noise

We assessed the effects of noise on the behavior of a model hair bundle crossing either a subcritical or a supercritical Hopf bifurcation. To achieve this we calculated the frequency of spontaneous oscillation as a function of the control parameter for two levels of noise and two peak-detection thresholds (Fig. S13).

When subjected to increasing values of constant force, a model hair bundle with a stiffness of 2 crossed a subcritical Hopf bifurcation (Fig. S13A, [3]). At high values of the constant force the bundle exhibited no spontaneous activity. Decreasing the constant force below a critical value caused a sudden onset of limit-cycle oscillations that corresponded to a discontinuous jump in frequency in the absence of noise. The frequency then rose slowly with further decreases in the constant force. When noise was added, the discontinuity in frequency disappeared and the bundle's oscillations decreased gradually to zero with increased force. Raising the level of noise caused the bundle to oscillate spontaneously at larger values of constant force, indicating that a hair bundle may exhibit spontaneous oscillations far from the deterministic subcritical Hopf bifurcation. Finally, changing the value of the peak-detection threshold caused no changes in the relationship between frequency and constant force.

A model hair bundle subjected to a constant force of 0 and increasing values of stiffness instead crossed a supercritical Hopf bifurcation (Fig. S13B, [3]). When the stiffness was large, the bundle exhibited no spontaneous motion in the absence of noise. Upon reduction of the stiffness below a critical value, limit-cycle oscillations emerged at a non-zero frequency. Further decreases in the stiffness caused a decline in the bundle's frequency of oscillation. As for a bundle operating near a subcritical Hopf bifurcation, adding noise to the system obscured the discontinuity in the relationship between frequency and stiffness. Unlike that of a subcritical Hopf bifurcation, however, the frequency relationship shifted rightward with an increase in the peak-detection threshold value.

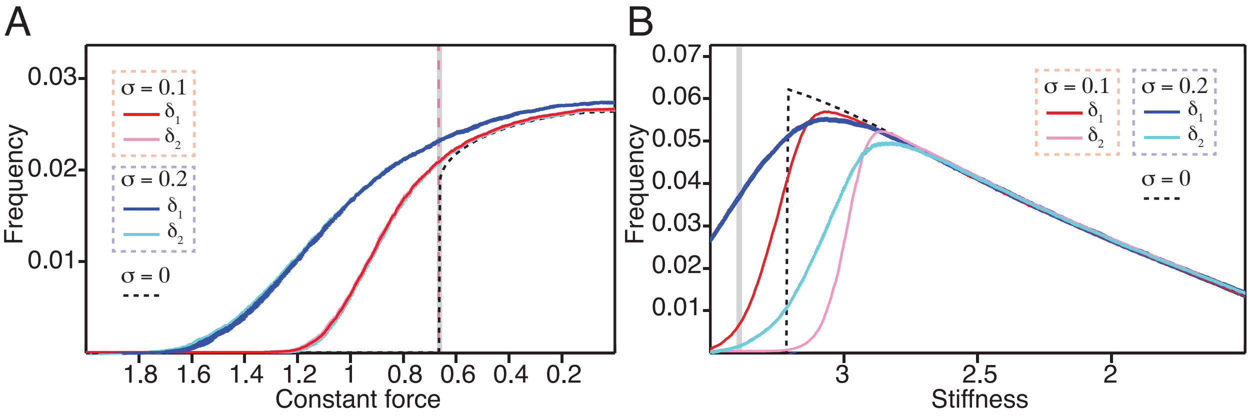

Figure S13: **Effects of noise on a model hair bundle's frequency of oscillation.** (A) A model hair bundle was poised at a stiffness of 2 and subjected to an array of 500 constant forces ranging from 0 through 2 such that the bundle crossed a subcritical Hopf bifurcation (gray line). In the absence of noise, the bundle exhibited spontaneous oscillations whose frequency rose discontinuously at a critical value of the constant force (black dashed line). The slope of the frequency relationship decreased as a function of noise level, obscuring the discontinuity (solid lines). Changes to the peak-detection threshold did not appreciably alter the frequency relationship. A saddle-node of limit cycles bifurcation occurred at $F_C = 0.664$ (pink dashed line). (B) A model bundle was poised at a constant force of 0 and subjected to 500 stiffnesses ranging from 1.5 through 3.5 such that the bundle crossed a supercritical Hopf bifurcation (gray line). In the absence of noise, spontaneous oscillations emerged with a non-zero frequency at a critical value of the total stiffness and the frequency of oscillation fell with decreased stiffness (dashed line). Adding noise reduced the slope of the rise in frequency (solid lines). Increasing the peak-detection threshold shifted the frequency curves rightward. All error bars represent standard errors of the means from five time series. We employed thresholds of $\delta_1 = 1$ and $\delta_2 = 1.5$. Deterministic plots were calculated with a threshold of 10^{-3} in both panels.

SECTION F

Analysis of Hair Bundles in the Presence of Noise

We found that hair bundles exhibited at least two classes of behavior that corresponded to operation near distinct bifurcations. Here we include extended time-series data that correspond to these two regimes.

F.1 Operation Near a Supercritical Hopf Bifurcation

A hair bundle subjected to a large load stiffness and a constant force of 0 displayed behaviors consistent with those of a system near a supercritical Hopf bifurcation (Fig. S14A). As the load stiffness fell, the bundle's amplitude of spontaneous oscillation increased. We additionally observed a decline in the frequency of oscillation that agreed with simulations of a model of hair-bundle dynamics (Fig. S13B). The joint probability distribution of the bundle's position and the Hilbert transform of its position possessed a circular region that increased in diameter with a decrease in load stiffness.

F.2 Operation Near a SNIC or Subcritical Hopf Bifurcation

Subjecting another bundle to a small load stiffness and a range of constant forces evoked behaviors that accorded with operation near either a SNIC or a subcritical Hopf bifurcation (Fig. S14B). A decrease in constant force caused the bundle to exhibit asymmetric oscillations with downward excursions that resembled spikes. The interval between successive excursions fell with a decrease in constant force. Joint probability distributions of the bundle's position and its Hilbert transform disclosed a limit cycle whose diameter remained invariant to changes in constant force. A region of high probability additionally existed on the limit cycle. Although we expected the bundle to cross a subcritical Hopf bifurcation in the low-stiffness regime [3], the behavior instead resembled that of a system near a SNIC bifurcation. We noted, however, that the same behaviors arose in our model of hair-bundle mechanics when noise was added to the system (Figs. 5, S13A). We therefore hypothesize that a hair bundle crossing a subcritical Hopf bifurcation can exhibit behaviors resembling those of a system near a SNIC bifurcation. We further explore this phenomenon in Figures 4 and 5.

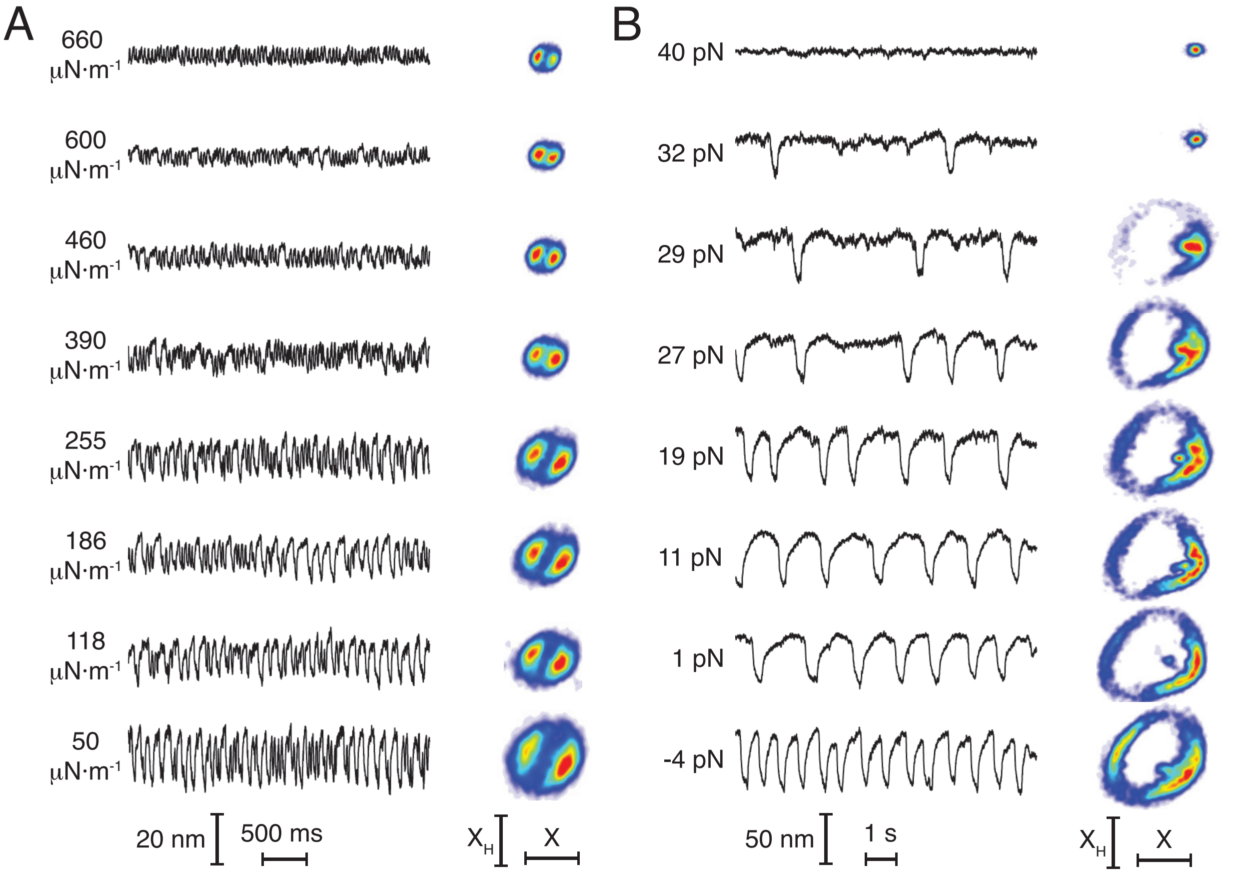

Figure S14: **Two classes of hair-bundle behavior.** (A) While subjecting a hair bundle to a constant force of 0 and load stiffnesses ranging from 50 $\mu N \cdot m^{-1}$ through 660 $\mu N \cdot m^{-1}$, we monitored its position over the course of 30 s under each condition. We display a 3.5 s window of each time series. (left) The bundle oscillated spontaneously with high frequency and low amplitude at a load stiffness of 660 $\mu N \cdot m^{-1}$. Reducing the load stiffness caused the bundle's oscillations to decrease in frequency and increase in amplitude. (right) The distributions of the bundle's position X and its Hilbert transform X_H based on 30 s of data revealed a limit cycle whose diameter rose with a decrease in load stiffness. (B) We subjected a second hair bundle to a load stiffness of 50 $\mu N \cdot m^{-1}$ and constant forces ranging from -4 pN to 40 pN and tracked its motion over a course of 30 s under each condition, and we display a 10 s window of each time series. Subjecting the bundle to a constant force of 40 pN suppressed its spontaneous activity (left). Decreasing the force caused downward excursions to emerge at a low frequency; further declines in the constant force increased the frequency of these excursions. Distributions of the bundle's position X and its Hilbert transform X_H based on 30 s of data indicated the presence of a single fixed point at a constant force of 40 pN (right). Reducing the force to 29 pN unveiled a limit cycle upon which rested a region of high probability. Further decreases in constant force caused the bundle to reside with greater probability at other positions along the cycle. For forces below 19 pN, a region of high probability appeared within the cycle. All data were acquired at sampling intervals of 1 ms. The stimulus fiber possessed a stiffness of 260 $\mu N \cdot m^{-1}$ and a drag coefficient of 130 $nN \cdot s \cdot m^{-1}$.

SECTION G

Noise-Induced Spiking in a Model of Hair-Bundle Mechanics

We hypothesized that a hair bundle achieves behaviors resembling those of a system near a SNIC bifurcation through an asymmetry in its phase space and quasi-threshold phenomena similar to those in models of spiking neurons [20, 21, 22]. In other words, a bundle could exhibit noise-induced excursions resembling all-or-none spikes in the quiescent regime at small stiffnesses. We assessed this possibility by analyzing the vector fields for a model hair bundle within different regions of its state space.

G.1 Effects of Constant Force and Stiffness

We first assessed the vector fields of our model of hair-bundle dynamics when the bundle was subjected to a low stiffness and increasing values of constant force. When its operating point rested on the oscillatory side of a subcritical Hopf bifurcation, the bundle exhibited limit-cycle oscillations (Figs. S15A-B). All trajectories proceeded toward a stable limit cycle in which the bundle displayed relaxation oscillations. The slow parts of each cycle corresponded to trajectories that fell near the cubic $\dot{X} = 0$ nullcline and the fast parts to rapid jumps across this nullcline's middle region. An unstable fixed point was situated at the intersection of the cubic $\dot{X} = 0$ and linear $\dot{f} = 0$ nullclines. An increase in the constant force caused the cubic nullcline to migrate in the positive X- and f-directions until the fixed point became stable at a subcritical Hopf bifurcation and the limit-cycle attractor subsequently disappeared at the nearby saddle-node of limit cycles (Figs. S15B-C). This behavior closely resembled the excitation-block phenomenon in models of neuronal dynamics [23]. After the bundle's operating point crossed a subcritical Hopf bifurcation and the subsequent saddle-node of limit cycles bifurcation, the bundle's trajectories converged on a stable fixed point (Fig. S15C). Trajectories diverged sharply from a region near and above the middle part of the cubic nullcline. If the hair bundle's trajectory were to cross this quasi-threshold region, the trajectory would correspond to a large-amplitude excursion in X as it extended toward one of the cubic nullcline's side branches [20, 24, 25]. Further increases in constant force propelled the stable fixed point farther from the middle branch of the cubic nullcline (Fig. S15D). By increasing the distance between the stable fixed point and the quasi-threshold region, a larger perturbation would be required to move the bundle's trajectory beyond the quasi-threshold.

We next assessed the behavior of a model hair bundle subjected to a constant force of zero and increasing values of stiffness. As the bundle's stiffness increased and its operating point approached a supercritical Hopf bifurcation, the slope of the middle branch of the $\dot{X} = 0$ nullcline fell (Figs. S16A-B). This caused the diameter of the limit cycle to decline with an increase in stiffness. On the quiescent side of the deterministic bifurcation, the slope of the middle branch of the $\dot{X} = 0$ nullcline became negative, rendering its fixed point stable (Figs. S16C-D). Because in the quiescent regime there existed no divergent trajectories near the $\dot{X} = 0$ nullcline, no quasi-threshold existed.

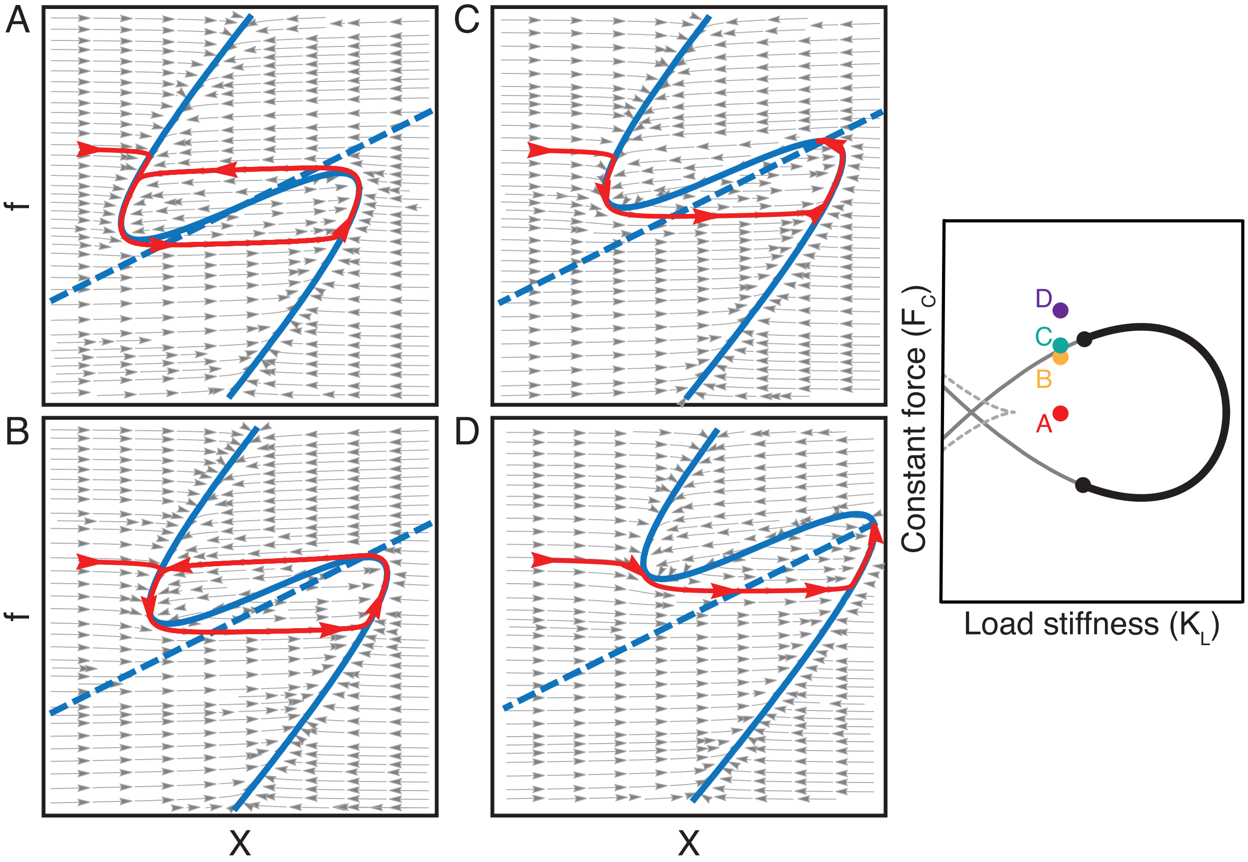

Figure S15: **Vector fields for a model hair bundle as a function of constant force.** We calculated the vector fields in the bundle's position X and the adaptive force f from Equations S31 and S32. As depicted in the panel on the right, we subjected the hair bundle to a stiffness of 2 and constant forces of 0 (A), 0.6 (B), 0.7 (C), and 1.5 (D); the bundle's operating point crossed a subcritical Hopf bifurcation at a constant force of 0.66. A fixed point resided at the intersection of the $\dot{X} = 0$ (solid blue) and $\dot{f} = 0$ (dashed blue) nullclines. Gray arrows indicate the local directions of trajectories. Although trajectories always cross the X nullcline vertically and the f nullcline horizontally, the region over which this occurs is often too small for the trajectories' directions to be represented accurately by the arrows. Red curves and arrows highlight example trajectories in the absence of noise. All panels were generated in Mathematica (10.2.0.0).

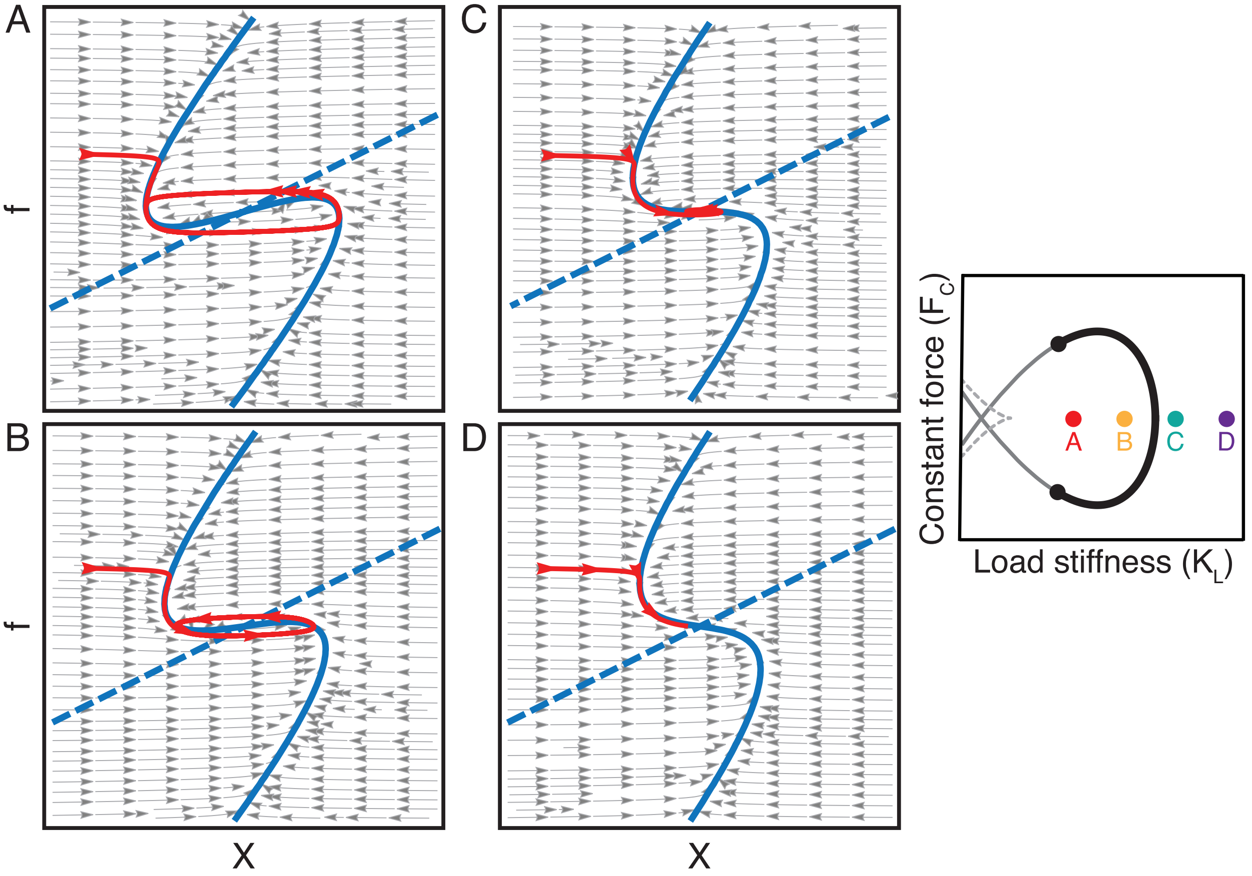

Figure S16: **Vector fields for a model hair bundle as a function of stiffness.** We calculated the vector fields in the bundle's position X and the adaptive force f. As shown in the rightmost panel, we subjected the hair bundle to a constant force of 0 and stiffnesses of 2.5 (A), 3 (B), 3.5 (C), and 4 (D); the bundle's operating point crossed a supercritical Hopf bifurcation at a stiffness of 3.4. A fixed point resided at the intersection of the $\dot{X} = 0$ (solid blue) and $\dot{f} = 0$ (dashed blue) nullclines. Gray arrows indicate the trajectories' local directions. Red curves and arrows highlight example trajectories in the absence of noise. All panels were generated in Mathematica (10.2.0.0).

G.2 Quasi-Threshold Behavior in a Bundle Model

We hypothesized that a hair bundle's stiffness and constant force control its capacity to exhibit large-amplitude spikes in the presence of noise. To assess this possibility, we simulated a hair bundle's response to shocks—instantaneous changes in X—that mimicked noisy perturbations to the bundle's position starting at the system's stable fixed point (Fig. S17). These shocks could induce excursions that appeared to be all-or-none spikes arising from quasi-thresholds in the bundle's phase portrait. Unlike a true threshold with a well-defined boundary, a quasi-threshold corresponds to a region near a stable fixed point in which nearby trajectories can diverge from one another. All shocks that exceed the quasi-threshold region cause large excursions of indistinguishable amplitudes. For this reason, crossing a quasi-threshold leads to a behavior similar to the that obtained by crossing a true threshold. A quasi-threshold region may be so narrow that it becomes difficult to distinguish it from a true threshold. A classic example of this phenomenon can be found in the Hodgkin-Huxley model of neurons, in which large-amplitude excursions resembling all-or-none spikes arise from quasi-threshold behavior [21, 23].

We searched for a quasi-threshold's location by manually iterating through different shock magnitudes and defined the quasi-threshold as the value of X at which trajectories diverged from one another and beyond which a family of trajectories possessed amplitudes that were indistinguishable from one another within a certain resolution. When the stiffness was low and the bundle operated closer to a subcritical Hopf bifurcation, the bundle exhibited a large-amplitude spike if the shock exceeded a quasi-threshold over a broad range of constant forces. Increasing the bundle's stiffness caused the spike amplitude to fall and the range of constant forces over which quasi-threshold behavior could occur to decrease, but the magnitude of the shock required to exceed the quasi-threshold shrunk owing to the fact that the bundle's operating point resided closer to a Hopf bifurcation. When the stiffness was high and the bundle operated closer to a supercritical Hopf bifurcation, no quasi-threshold was found for shocks in X across all constant forces. Here the bundle rang in response to a shock with an amplitude that grew with the shock's magnitude.

Quasi-threshold phenomena in a bundle's response to shocks arose from its specific dynamics rather than the behavior of a system described by the normal form of a subcritical Hopf bifurcation. To illustrate these dynamics, we calculated a hair bundle's response to shocks in phase space using the same parameters as before. Increases in a bundle's constant force induced translation of the $\dot{X} = 0$ nullcline, causing the stable fixed point to move farther from the location of a quasi-threshold in the X-direction (Fig. S18). Shocks of larger magnitude were therefore required to induce a spike as the constant force rose. When the constant force was very large, the bundle's fixed point fell below the middle branch of the $\dot{X} = 0$ nullcline. Increasing a bundle's stiffness caused the middle part of the $\dot{X} = 0$ nullcline to become shallower. This had two effects. First, the amplitude of shock-induced spikes decreased as the stiffness rose. Second, nearby trajectories no longer diverged as sharply from a region near the middle branch of the $\dot{X} = 0$ nullcline. As a result, the range of constant forces over which a quasi-threshold existed fell with an increase in stiffness. No quasi-threshold was found for shocks in X across all constant forces at stiffnesses of 2.6 and 3.0.

Noise can induce shocks in the f as well as the X direction. A quasi-threshold thus corresponds to an area in the bundle's phase portrait. For illustration, we analyzed shocks in only the X direction rather than in both the X and f directions. Noise-induced excursions resembling all-or-none spikes therefore arise from a quasi-threshold in a hair bundle's phase space. These spikes achieve similar amplitudes and can be elicited over a broader range of constant forces when the bundle's operating point lies in the low-stiffness regime. The spike amplitude additionally increases for smaller stiffness values. Finally, the perturbation size required for a bundle to spike falls as changes in constant force bring the system's operating point toward a line of subcritical Hopf bifurcations.

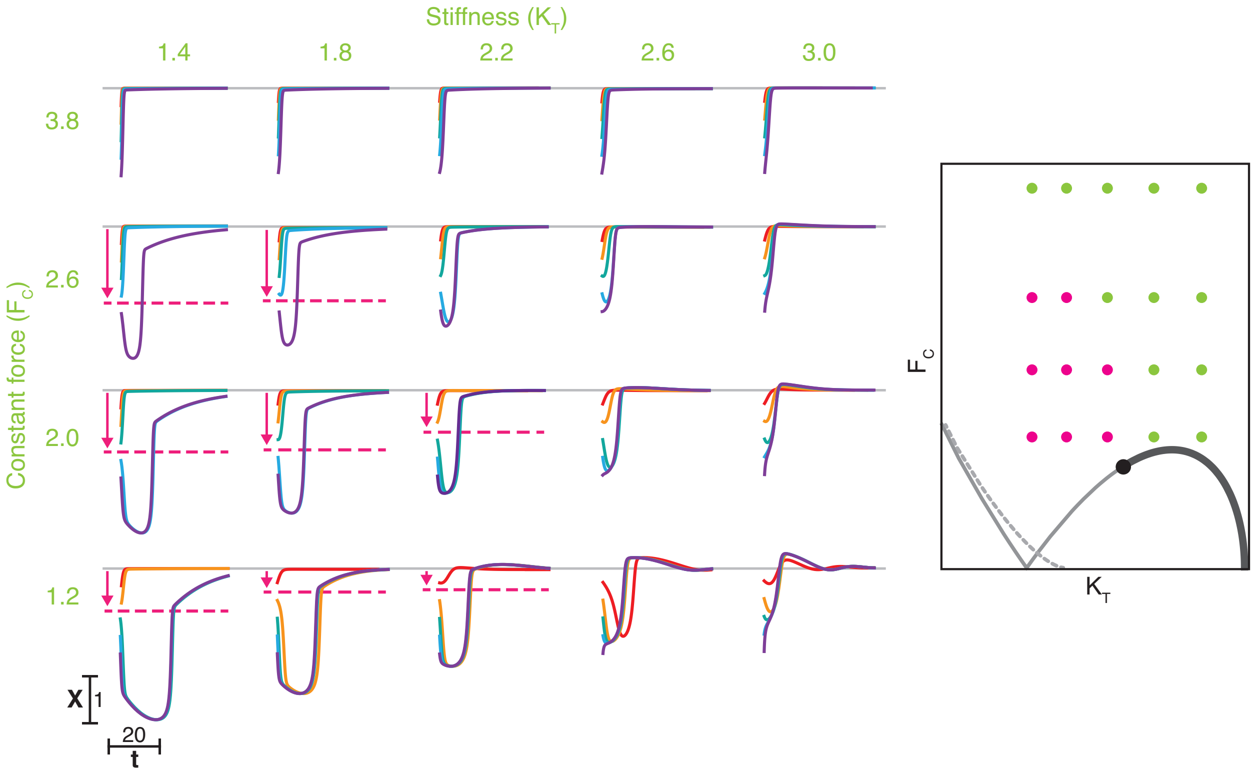

Figure S17: **Time series of a model bundle's response to instantaneous changes in its position.** A model hair bundle was subjected to constant forces of $F_C = \{1.2, 2.0, 2.6, 3.8\}$ and stiffnesses of $K_T = \{1.4, 1.8, 2.2, 2.6, 3.0\}$. The locations of these operating points are represented in the schematic state diagram on the right, in which dashed, thin, and thick lines correspond respectively to lines of fold, subcritical Hopf, and supercritical Hopf bifurcations. Pink circles correspond to those operating points at which a quasi-threshold was found. At each operating point, the bundle's dynamics was simulated using five different initial conditions. Each initial condition corresponded to the fixed-point value for f but to different values for X, each separated by $\Delta X = 0.4$ (red to purple). Pink dashed lines and arrows correspond to the approximate location in X of a quasi-threshold. If the bundle's position exceeded the quasi-threshold, the bundle exhibited a large-amplitude excursion that resembled an all-or-none spike. The distance between the bundle's steady-state position and the quasi-threshold at a given stiffness rose with an increase in constant force. No quasi-threshold existed for the constant forces shown at stiffness values of 2.6 and 3.0. In the absence of a quasi-threshold, the bundle instead exhibited ringing with an amplitude that grew with the bundle's initial position. All simulations were generated from Equations S31 and S32 in Mathematica (10.2.0.0).

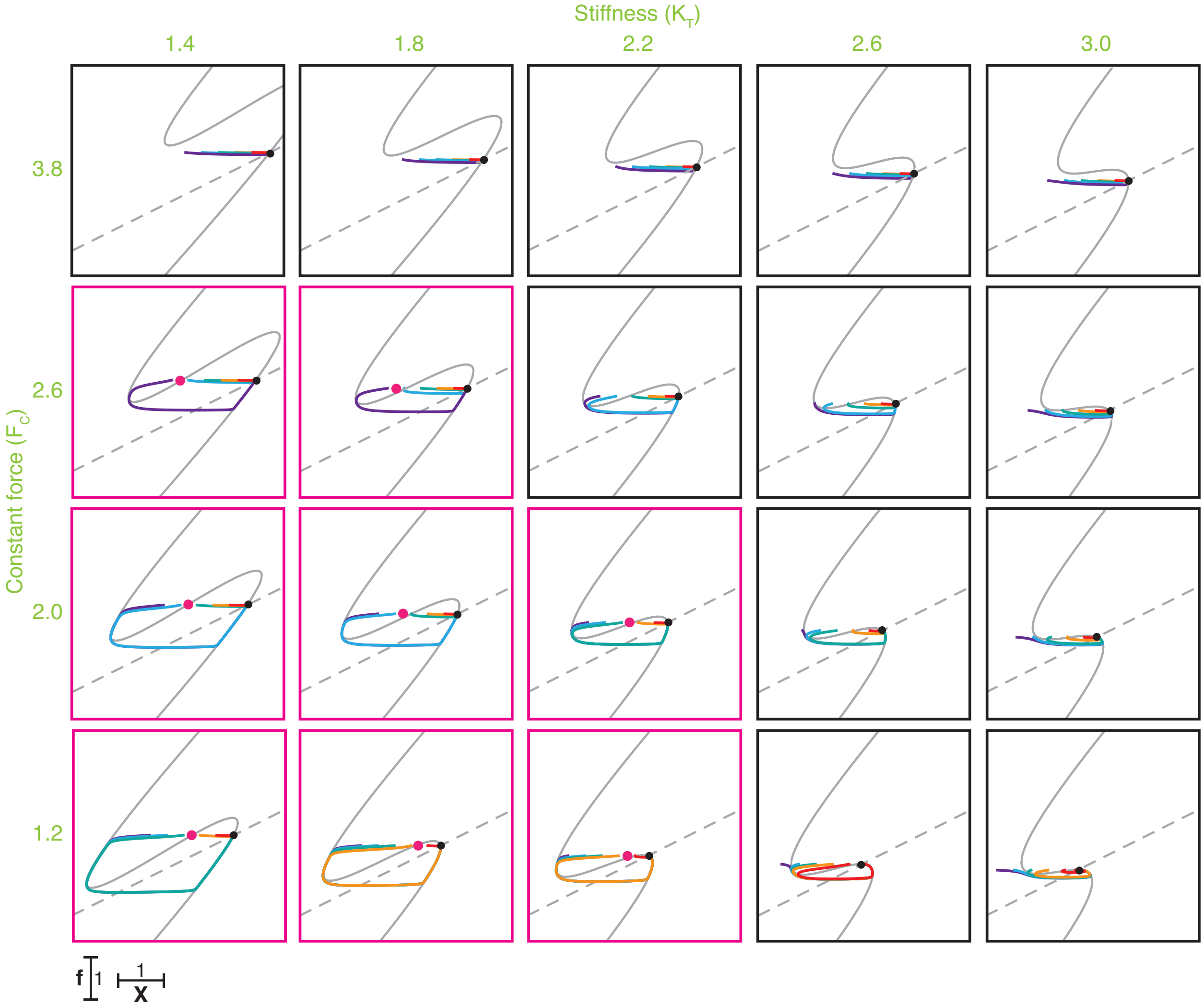

Figure S18: **Phase portraits of a model bundle's response to instantaneous changes in its position.** Using the same parameters as for Fig. S17, we simulated a model hair bundle's trajectory in phase space. Solid and dashed gray lines correspond respectively to the $\dot{X} = 0$ and $\dot{f} = 0$ nullclines. Black circles at the intersection of these nullclines correspond to stable fixed points. Pink circles approximate the location of a quasi-threshold. Those operating points for which a quasi-threshold existed are outlined in pink. Each colored curve represents the bundle's trajectory starting at a fixed value of f and increasing initial positions in X (red to purple). All trajectories evolved to eventually reside at the stable fixed point for each operating point. Increases in constant force shifted the $\dot{X} = 0$ nullcline in the positive X- and f-directions. This caused the distance between the bundle's stable fixed point and its quasi-threshold to grow. When the constant force increased to 3.8 the fixed point fell below the middle part of the $\dot{X} = 0$ nullcline, rendering the quasi-threshold inaccessible to shocks in the bundle's position X. As the stiffness increased, the slope of the middle part of the $\dot{X} = 0$ nullcline declined, causing the magnitude of shock-induced spikes to decrease and the range of constant forces over which a quasi-threshold existed to fall. No quasi-threshold in the X-direction existed for any value of constant force at stiffnesses of 2.6 and 3.0. All simulations were generated from Equations S31 and S32 in Mathematica (10.2.0.0).

References

[1] Salvi, J. D., D. Ó Maoiléidigh, B. A. Fabella, M. Tobin, and A. J. Hudspeth. 2015. Characterization of Active Hair-Bundle Motility by a Mechanical-Load Clamp. In K. D. Karavitaki and D. P. Corey (Eds.), Mechanics of Hearing: Protein to Perception, pages 030005:1–5.

[2] Salvi, J. D., D. Ó Maoiléidigh, B. A. Fabella, M. Tobin, and A. J. Hudspeth. 2015. Control of a hair bundle's mechanosensory function by its mechanical load. Proceedings of the National Academy of Sciences 112(9):E1000–9.

[3] Ó Maoiléidigh, D., E. M. Nicola, and A. J. Hudpseth. 2012. The diverse effects of mechanical loading on active hair bundles. Proceedings of the National Academy of Sciences of the United States of America 109(6):1943–1948.

[4] Bormuth, V., J. Barral, J.-F. Joanny, F. Jülicher, and P. Martin. 2014. Transduction channels' gating can control friction on vibrating hair-cell bundles in the ear. Proceedings of the National Academy of Sciences of the United States of America 111(20):7185–7190.

[5] Hartigan, J. A. and P. M. Hartigan. 1985. The dip test of unimodality. The Annals of Statistics 13(1):70–84.

[6] Freedman, D. and P. Diaconis. 1981. On the histogram as a density estimator: L2 theory. Probability Theory and Related Fields (Heidelberg: Springer Berlin) 57(4):453–476.

[7] Jacobson, M. L. 2001. Auto-Threshold Peak Detection in Physiological Signals. 23rd Annual International Conference of the IEEE Engineering in Medicine and Biology Society pages 1–4.

[8] Whitney, H. 1936. Differential manifolds. Annals of Mathematics 37(3):645–680.

[9] Takens, F. 1981. Detecting strange attractors in turbulence. Lecture Notes in Mathematics 898.

[10] Kennell, M. B. and H. D. I. Abarbanel. 2002. False neighbors and false strands: A reliable minimum embedding dimension algorithm. Physical Review E 66:026209.

[11] Fraser, A. M. and H. L. Swinney. 1986. Independent coordinates for strange attractors from mutual information. Physical Review A 33(2):1134–1140.

[12] Sauer, T., J. A. Yorke, and M. Casdagli. 1991. Embedology. Journal of Statistical Physics 65(3):579–616.

[13] Kralemann, B., L. Cimponeriu, M. Rosenblum, A. Pikovsky, and R. Mrowka. 2007. Uncovering interaction of coupled oscillators from data. Physical Review E 76(055201(R)):1–4.

[14] Kralemann, B., L. Cimponeriu, M. Rosenblum, A. Pikovsky, and R. Mrowka. 2008. Phase dynamics of coupled oscillators reconstructed from data. Physical Review E 77(066205):1–16.

[15] Zhu, Y., Y.-H. Hsieh, R. R. Dhingra, T. E. Dick, F. J. Jacono, and R. F. Galán. 2013. Quantifying interactions between real oscillators with information theory and phase models: Application to cardiorespiratory coupling. Physical Review E 87(2):022709.

[16] Ermentrout, G. B. and N. Kopell. 1986. Parabolic bursting in an excitable system coupled with a slow oscillation. SIAM Journal on Applied Mathematics 46(2):233–253.

[17] Ermentrout, B. 1996. Type I membranes, phase resetting curves, and synchrony. Neural Computation 8(5):979–1001.

[18] McKennoch, S., T. Voegtlin, and L. Bushnell. 2008. Spike-timing error backpropagation in theta neuron networks. Neural Computation 21(1):9–45.

[19] Kuznetsov, Y. 2004. Elements of Applied Bifurcation Theory. Applied Mathematical Sciences. Springer.

[20] FitzHugh, R. 1955. Mathematical models of threshold phenomena in the nerve membrane. Bulletin of Mathematical Biophysics 17(4):257–278.

[21] Izhikevich, E. M. 2000. Neural excitability, spiking and bursting. International Journal of Bifurcation and Chaos 10(6):1171–1266.

[22] Rinzel, J. and G. B. Ermentrout. 1989. Analysis of neural excitability and oscillations. Methods in neuronal modeling: From synapses to networks. MIT Press (Cambridge, MA).

[23] Izhikevich, E. M. 2007. Dynamical Systems in Neuroscience: The Geometry of Excitability. The MIT Press (Cambridge, MA).

[24] Treutlein, H. and K. Schulten. 1985. Noise induced limit cycles of the bonhoeffer-van der pol model of neural pulses. Berichte der Bunsen-Gesellschaft für Physikalische Chemie 89:710–718.

[25] Lindner, B., J. García-Ojalvo, A. Neiman, and L. Schimansky-Geier. 2004. Effects of noise in excitable systems. Physics Reports 392:321–424.